POLITECNICO DI TORINO

Master Course
in Mathematical Engineering

Master's Degree Thesis

A machine learning-based reduced order model for the investigation of the blood flow patterns in presence of a stenosis of the left main coronary artery

Advisor
Prof. Claudio Canuto
Prof. Gianluigi Rozza

Co-Advisor
Dr. Francesco Ballarin
Dr. Michele Girfoglio

Candidate
Pierfrancesco Siena

Academic Year 2020-2021

Alla nonna Maria, sempre vicina

in ogni traguardo della mia vita.

Abstract

Coronary artery diseases represent a significant cause of death worldwide. In fact, their occlusion can cause lack of oxygen to the heart tissue, leading to heart failure or heart attack. Coronary artery bypass grafting is a surgical procedure to restore a proper blood supply. In this context, Computational Fluid Dynamics (CFD) can be a significant tool to improve coronary artery bypass grafts and to avoid unfavorable flow conditions in the region of the anastomosis, which can be associated with the failure of the surgical procedure.

In this thesis the development of a Reduced Order Model (ROM) for the investigation of hemodynamics in a patient-specific configuration of coronary artery bypass graft is proposed. The method deployed extracts a reduced basis space from a collection of high-fidelity solutions via a Proper Orthogonal Decomposition (POD) algorithm and employs Artificial Neural Networks (ANN) for the computation of the modal coefficients. The main goal is to characterize blood flow for different settings that are relevant in the clinical practice, such as several stenosis factors, in a rapid and reliable way. The Full Order Model (FOM) is represented by the incompressible Navier-Stokes equations discretized by using a Finite Volume (FV) technique. The computational domain is referred to coronary arteries, in particular left branches when a stenosis of the Left Main Coronary Artery (LMCA) occurs.

In the first stage, only a stenosis that reduces the width of the vessel by 50% is taken into account, so the time is the only parameter considered in the model. Then, stenosis from mild to severe is added too. Several numerical results are analysed, underlining the computational performance of the proposed approach, such as the error between computed FOM and ROM solutions as well as the substantial speed-up achieved at the online stage.

Acknowledgements

This thesis has been developed in collaboration between SISSA mathLab and Sacco hospital of Milan. First of all, I would like to thank you my thesis advisor Prof. Claudio Canuto of Politecnico di Torino for giving me the opportunity to work on this project and to know this challenging place. A very special thank you goes to Prof. Gianluigi Rozza of Scuola Internazionale Superiore di Studi Avanzati (SISSA) for his availability and his kindness during this gorgeous period I spent in SISSA. A huge thank you goes to Dr. Michele Girfoglio and Dr. Francesco Ballarin for their patience and professionalism in solving my problems and listening my doubts. I am grateful also to Ospedale Luigi Sacco, in particular to Dr. Roberto Scrofani for providing clinical configurations of interest for this thesis. Finally, I would like to acknowledge the support provided by the European Research Council Executive Agency by the Consolidator Grant project AROMA-CFD "Advanced Reduced Order Methods with Applications in Computational Fluid Dynamics" - GA 681447, H2020-ERC CoG 2015 AROMA-CFD.

Contents

List of Tables

List of Figures

Introduction

When severe coronary artery diseases occur, one or more coronary arteries are occluded causing a poor perfusion of oxygen-rich blood to the heart. Coronary artery bypass grafting is still one of the most used surgical procedure worldwide, although after some years blood supply fails again, causing the need of reintervention. Investigating blood flow features near the anastomosis is of remarkable clinical interest, because some fluid dynamic indicators are related to restenosis and they can be estimated by means of numerical simulations. Therefore, several computational hemodynamic studies have been performed during the last years. High fidelity simulations for each new parameter are unfeasible and reduced order models are applied to avoid this problem. In fact, reduced order models enable fast computations varying the parameters, as often required in the clinical context, and they aim at a possible improvement of the surgical operation. In this thesis computational reduction techniques are developed, focusing on patient specific geometries.
Reduced order models and *machine learning* are two key words of the thesis. In the last years reduced order models have been applied in many different fields, allowing to obtain an accurate description of the system with a significant reduction of the computational cost. In addition, recently, machine learning and artificial intelligence seem to have an increasing impact in many different areas. So, proper orthogonal decomposition - neural network (POD-NN) method is considered in this thesis.
A finite volume discretization is employed on high performance computing facilities. Then, the basis functions are computed from the snapshots of the full order model. In particular, artificial neural networks are employed to accurately approximate the coefficients of the reduced solution.
The structure of the thesis is as follows. Chapter 1 provides an overview of the clinical problem. The anatomy of coronary arteries is deployed, focusing on the main branches. Afterwords, atherosclerosis, which is the main disease of coronary vessels, with some possible surgical treatments, is presented. Some papers are discussed in order to understand better the reasons and the geometries of our work. Finally, the importance of mathematical investigation on this topic is highlighted.
Chapter 2 contains a description of the blood components and a discussion about some models used to describe the blood flow. It is useful to justify the use of a Newtonian model. Then, we introduce the strong formulation of incompressible Navier-Stokes equations, explaining how the assumptions modify the model. In the last section, boundary conditions are introduced, focusing on realistic flow rate waveform obtained from literature.

Chapter 3 deals with the finite volume method. In particular, it is analysed the discretization of the domain, trying to minimize errors due to the grid. Then, in order to ensure that the finite volume model converges to a solution, a mesh convergence analysis is carried out.
Chapter 4 deals with the computational reduction framework and presents several results on the patient specific bypass graft configuration. A POD-NN model is introduced and operations performed during offline/online stages are specified. In addition, a detailed justification for the use of this method is deployed. Qualitative and quantitative results for time and for stenosis degree reduction are shown, comparing full-order and reduced-order solutions.
Finally, some conclusions and an outlook of possible future research conclude this thesis.

Chapter 1

Cardiovascular system

In the first section, we introduce some basic knowledges about the cardiovascular system, focusing on the coronary arteries, in order to understand structures and connections of the vessels. It will be done also a general overview about the main diseases of the coronary arteries with notes on the most used surgical procedures. This chapter is not intended to be a complete discussion of coronary anatomy and pathology. The goal is to understand better the problem and to underline the importance of mathematical investigation on this topic. Finally, it is specified the problem of our interest, which will be developed in collaboration with Sacco hospital in Milan.

1.1 Anatomy of coronary arteries

Coronary arteries form a network of vessels that wrap around the entire heart. Their main function is to supply oxygenated blood to the myocardium. Because the myocardium lacks the ability to contract anaerobically, the constant supply of oxygen by the coronary vessels is crucial for the regular function of the heart [1].
The arrangement of coronary arteries varies considerably among people, for this reason in our work the real geometry of the patient will be extracted from medical images. In the following, we briefly analyse the main branches, without focusing on the individual differences.
The right coronary artery (RCA) and the left main coronary artery (LMCA) are the first two branches of the coronary arteries and both originate from the root of the aorta.
The RCA emerges from the anterior ascending aorta and supplies blood mainly to the right atrium and right ventricle. Then, the RCA typically divides into smaller branches: the right posterior descending artery (PDA) and the right marginal artery. The posterior descending artery supplies oxygenated blood to the posterior one-third of the interventricular septum. The left anterior descending artery (LAD) is responsible for the anterior two-thirds of the septum. Actually, the supply of interventricular septum was estimated to be different in each heart, as better specified in [23].
The LAD is one of two major branches of the LMCA, the other is the left circumflex (LCx) coronary artery. Together, these two branches supply blood to the left atrium and

left ventricle. The circumflex artery provides blood supply to the left atrium and the posterior-lateral part of the left ventricle, while the LAD supplies blood to the anterior portion of the left ventricle [22]. For the sake of clarity, anatomy described is shown in Figure 1.1 and a more detailed explanation can be found in [36].

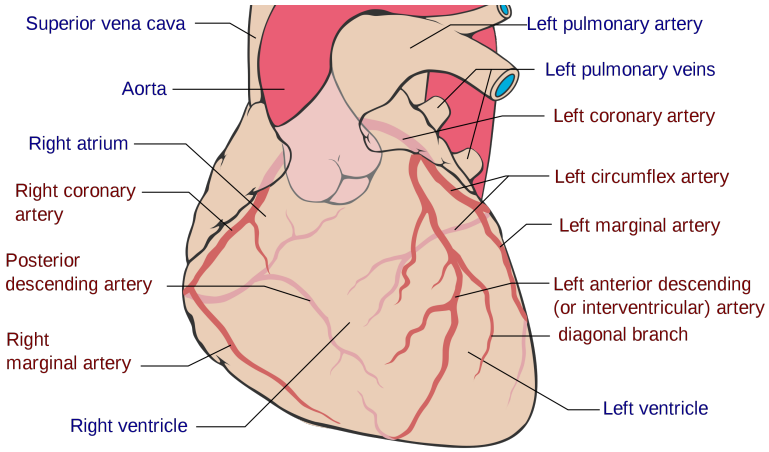

Figure 1.1: Diagram of coronary arteries.

1.2 Atherosclerosis

Cardiovascular diseases are the main cause of death worldwide. The world health organization estimates that 17.9 million people die each year for disorders of the heart and blood vessels, about 31% of all deaths in the world. These numbers are sufficient to justify research in this area.
The two major vascular diseases are aneurysm, which is briefly a gradual dilation of an arterial segment with a consequent possible haemorrhage, and atherosclerosis, which is the disease of interest in our work.
Atherosclerosis is the accumulation of fatty materials, fibrous elements and calcium in the arteries. It is a progressive disease that can take decades for the development of symptoms. The initial stages are completely benign, but as the lesion develops it can reduce the lumen of the vessel creating a stenosis that obstructs blood flow leading to clinical complications. Clinically dangerous is the development of thrombi or the rupture of the plaque leading to emboli which are deposited in downstream vessels causing infarctions [1].
Coronary stenosis can be classified according to their location:

- proximal stenosis literally means situated nearer to the center of the vessel under examination, in practice it is located at the beginning of the vessel,
- mid stenosis is located in the central region of the vessel,
- distal stenosis means away from the center of the vessel, in practice it is located at the end of the vessel,

- ostial stenosis is located at the bifurcation of the vessel. If it is a predivisional stenosis, it comes before the division.

Finally, it is possible to associate a degree of severity to each stenosis. If the level of obstruction is less than 50%, the stenosis is mild, between 50% and 70%, it is moderate (they are rarely symptomatic), then it is classified as severe [25]. It is important to clarify that in this work, if not specified, the severity of the stenosis refers to the diameter of the vessel and not to its area.

1.2.1 Treatments

A surgical procedure applied to severely stenotic arteries is grafting. There are two techniques: vessel replacement and bypass. Replacement (end-to-end anastomosis) involves removing the stenotic artery and replacing it with another vessel. Bypass (side-to-side anastomosis) provides an alternative route for blood to bypass the stenosis, which is left in place [1]. Grafts can be done using arteries or veins from the patient, commonly the following patch graft materials are utilized: internal thoracic artery (ITA), autologous pericardia and saphenous vein (SV). Internal thoracic artery closely mimics the characteristics of the native coronary artery, but it may be limited by the conduit harvest. On the contrary, the pericardium is easily harvested, but it promotes calcification and subsequent restenosis. The saphenous vein is favoured by a number of surgeons for its size and character, which allow simple creation of a funnel-shaped ostium. However, its elasticity may bring about a tendency to dilatation and it may result in long-term restenosis [26].
Practically, single or multiple bypass grafting are possible in order to restore a better perfusion flow. All grafts suffer from complications, 50% close within 10 years after surgery. The most common failures are due to thrombus formation, restenosis of the vessel and deterioration of the graft material. Anyway, there is very active research into the development of new materials for grafts, this is still an open question.
Another minimally invasive procedure is stenting, where a catheter is advanced from a peripheral artery to the site of the stenosis. The stenosis is generally disrupted by dilating it with a balloon (angioplasty) which expands a wire mesh stent used to support the vessel walls. A common problem with stents is restenosis, which occurs at a significant rate. Consequently metallic stents and biodegradable stents have been developed. Several types of drug-eluting stents have been tested in clinical trials to limit cell migration and proliferation in the region of the stent [1].
Both approaches (grafting and stenting) can be adopted to revascularize all stenotic vessels (complete revascularization) or it is possible to select only some conduits (incomplete revascularization).

1.3 State of the art

Many papers study different coronary stenosis in order to establish a good clinical treatment, especially in term of mid-long survival. In this section we report some clinical studies on stenosis of the common trunk and their main results in order to outline and to understand better the state of the art.

Patients with isolated stenosis of the left main coronary artery (LMCA) are considered in [24]. Results after surgical revascularization show that 86.8% of patients were alive and 71.7% were free of any intercurrent coronary event after four years. In particular, they observed that extracorporeal circulation times and aortic clamping times are factors of risk for coronary events. In some cases of reintervention, LMCA treatment consisted of angioplasty, but the conclusion of the investigator is that it should not be considered an alternative to surgery except in certain favourable situations. In addition, focusing on patients with ostial stenosis, no significant differences are found in term of survival.
Paper [26] focuses only on isolated ostial stenosis of the LMCA. The authors try to understand if, in this rare case, angioplasty is a viable alternative to traditional bypass. The long-term mortality after angioplasty is found to be about 8%. In particular, they found that non-ostial stenosis, stenosis extending beyond the proximal LMCA and calcification remain an absolute contraindication to angioplasty, so conventional bypass should remain the standard procedure for such patients. Otherwise, they observed that both age and poor left ventricle function are not contraindication for this approach.
Patients often do not have isolated stenosis, so it is important to evaluate the impact of completeness of revascularization and multiple bypass grafting. This is the purpose of [28], where it is shown that for short-term outcomes revascularization strategy does not have a significant impact. Otherwise, after about four years, multi-arterial coronary artery bypass grafting (MA-CABG) has a survival advantage compared with single-arterial coronary artery bypass grafting (SA-CABG). Similarly, complete revascularization achieves better results than incomplete revascularization. Of course, one single revascularization strategy cannot be applied to all patients; but we can tell that in young patients complete revascularization with multiple arterial conduits is ideal. As supported by [25], less complete revascularization is accepted to limit invasiveness. In this work, patients with RCA, LAD and LCx diseases are considered and both percutaneous and operative strategies have been followed. It can be observed that survival is less in patients with left main trunk stenosis with incomplete revascularization of the LCx and RCA, with high-grade stenosis in the LCx system, and with high-grade proximal RCA stenosis. Instead, diseases in the mid and distal RCA were risk factors for reintervention. So, even if left ITA-LAD graft is the most important part of the bypass operation for most patients, it does not fully compensate for the presence of diseases in other coronary systems.
In [29], the study demonstrates again the significant superiority of coronary artery bypass over percutaneous coronary intervention, especially in patients with complex three-vessel diseases. Only in left main diseases with amenable anatomy, percutaneous approach is an alternative option.
Finally [27] is the work closest to our interest. Two surgical approaches are compared for isolated predivisional stenosis of the left main coronary artery: bilateral internal thoracic artery grafts and ITA on the left anterior descending artery and saphenous vein on the circumflex system. The main finding is that the addition of a second ITA graft or of a SV graft to the first ITA does not lead to different long-term angiographic patency. In particular, the use of SV as a complementary graft to the circumflex system does not jeopardize long-term patency of the ITA-LAD graft. It is an interesting result even if the sample size is limited and the angiographic follow-up rate was not 100% due to the death of some patients. So, it reinforces the need for further studies in this area and it justifies

mathematical simulation, as explained better in the next section.

1.4 Importance of the mathematical formulation

Nowadays, mathematical simulations can support researchers in the analysis of the circulatory system in physiological and pathological situations. The increasing demand from the medical community for quantitative investigations of cardiovascular diseases gave an impulse to develop studies. Naturally, the first motivation for cardiovascular modelling is the diffusion of cardiovascular diseases, the largest cause of death worldwide, especially in the developed countries.
Many groups focused on simulations of blood flow through arterial grafts and reconstructed vascular segments in order to provide knowledge of flow behaviour and the applied stress fields. A better understanding of these factors is crucial to our understanding of the diseases and investigations on realistic geometries determined from medical imaging are useful to optimize surgical procedures.
Better understanding of the flow and stress in grafts and graft junctions will aid in surgical planning of grafting and may improve the lifetime of grafts.
Numerical models of vascular flows on coronary system can also provide a virtual experimental platform to be used as a training system for new vascular surgeons and they can give specific design indications for the realization of surgical operations. It can help the surgeon in understanding how different surgical solutions may affect blood circulation and guide the choice of the most appropriate procedure for a specific patient [1].

1.5 Our work

Our study focuses on the blood flow in the coronary system when an isolated stenosis of the LMCA occurs. Varying the severity of the stenosis, two configurations are analysed in order to restore a proper blood supply:

- a CABG (Coronary Artery Bypass Grafting) performed with LITA (Left Internal Thoracic Artery) on the LAD. In the following we refer to this with the abbreviation CABG1 (Figure 1.2a),
- a CABG performed with LITA to restore the flow in the LAD and one performed with RITA (Right Internal Thoracic Artery) or with the radial artery or with the SV to restore the flow in the LCx. In the following we refer to this with the abbreviation CABG2 (Figure 1.2b).

An isolated stenosis of the main trunk is rare, and there is not a sample of consolidated studies which allow to establish the most appropriate procedure to perform. Therefore, numerical simulations of vascular flow represent a tool of significant importance. Numerical models can provide specific indications for the flow, vessel patency and wall shear stress (WSS). It supports surgeons when they have to choose the most appropriate procedure for a specific patient.
Effectively data provided by Sacco hospital will be used by the SISSA mathLab team

in order to reconstruct a virtual 3D model to perform numerical simulations. The reconstruction of the geometry will be indicatively obtained starting from post-operative data. However, if they are compromised, we will opt for a reconstruction starting from pre-operative data, with virtual addition of vessels inserted to comply with the actual intervention.
Although numerical methods such as finite volumes and finite elements are known and widely used in order to find an accurate solution of the Navier Stokes equations, a reduced model will be developed in order to significantly reduce the time simulation. This aspect is fundamental when the aim is to find patient specific data for different flow conditions and for different geometric configurations.
In order to compare the flow properties for CABG1 and CABG2, a reduced method for numerical simulation based on machine learning algorithms is developed and it will be analysed in details in the following. In particular, it is interesting to consider a stenosis of variable degree, from mild to severe, on the geometry under examination. The variables of interest are velocity, pressure and WSS. Therefore, the following preliminary scenarios are defined:

- CABG1 in the case of mild stenosis,
- CABG1 in the case of severe stenosis,
- CABG2 in the case of mild stenosis,
- CABG2 in the case of severe stenosis.

The results obtained want to provide various possibilities of intervention to the medical specialist in a field where the bibliography does not currently provide exhaustive guidelines and / or standardized protocols.

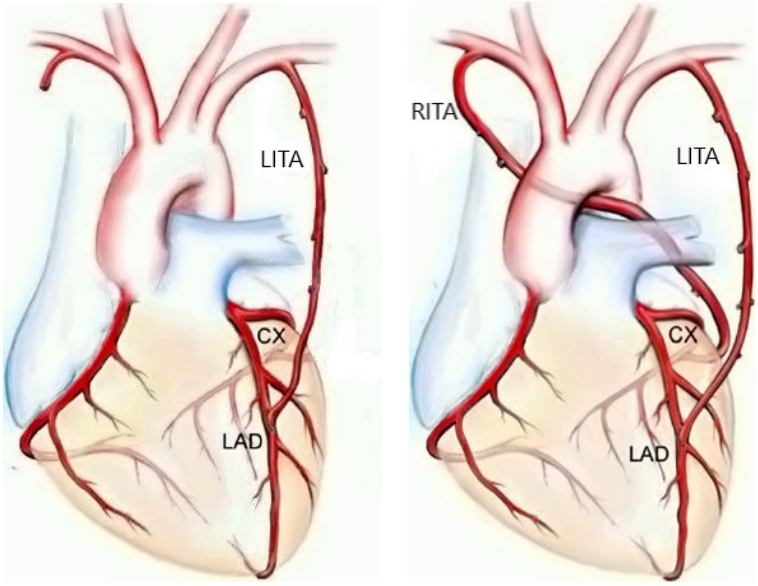

(a) CABG1. (b) CABG2.

Figure 1.2: Surgical approaches.

Chapter 2

The mathematical model

In this chapter, we introduce a mathematical model which describes the motion of viscous incompressible fluid substances, i.e. incompressible Navier-Stokes equations.
Firstly, we describe some features of the blood in order to understand better the assumptions about the fluid under consideration. It follows a discussion on the conservation of the momentum and the conservation of the mass, with a focus on boundary conditions.

2.1 Blood flow features

Blood is a suspension of cellular elements that includes red blood cells (RBCs) or erythrocytes, white blood cells (WBCs) or leukocytes and platelets or thrombocytes. They are suspended in an aqueous polymer solution, the plasma, containing electrolytes and organic molecules such as hormones, enzymes, antibodies, fibrinogen and other proteins. Erythrocytes exert the most significant influence on the mechanical properties of blood, due to their presence in very high concentration compared to the other elements, comprising about 45% of its volume in healthy individuals.
Although plasma is nearly Newtonian in behaviour, whole blood exhibits marked non-Newtonian characteristics, particularly at low shear rates. The non-Newtonian behaviour of blood is mainly explained by three phenomena:

- the propensity of the erythrocytes to form a three-dimensional microstructure at low shear rates,
- the deformability of erythrocytes,
- the tendency of erythrocytes to align with the flow field at high shear rates.

The macroscopic effect of the presence of RBCs is that blood is a shear-thinning fluid, it means that the viscosity decreases as the rate of deformation increases. Below a critical vessel calibre (about 1 mm), blood viscosity becomes dependent on the conduit radius and decreases sharply because red blood cells move to the central part of the capillary, whereas the plasma stays in contact with the vessel wall. This layer of plasma facilitates the movement of the red cells, thus causing a decrease of the apparent viscosity [1].

There are also others studies about non-Newtonian characteristics of the blood, such as [2], where the results show that fibrinogen causes the aggregation of RBCs with an increase in viscosity, preferentially at low shear rates.
Regardless, it is clear that blood is a non-Newtonian fluid, but the purpose of this section is to understand whether or not it is necessary to include non-Newtonian blood models in modelling blood flow in coronary arteries.
In [3] is presented a transient study of blood flow in four different human right coronary arteries with Newtonian model and Power blood (non-Newtonian) model. Comparing the two blood viscosity models shows that the non-Newtonian one is only significant for approximately 30% of the cardiac cycle. During these periods, the wall shear stress (WSS) is very low, with the regions of lowest WSS in the same positions for both models. Thus, it can be concluded that a Newtonian model for blood viscosity is an adequate approximation for transient simulations. Moreover, it appears that in terms of wall shear stress distribution, there is little practical difference between a Newtonian and a non-Newtonian model for blood viscosity. However, for simulation purposes, to study wall shear stress a Newtonian model would be satisfactory, but to study the flow in more detail, to look at mixing within the blood or stresses on individual blood cells for example, the non-Newtonian behaviour of the blood should be counted.
Also paper [4] compares some numerical results between two non-Newtonian models (Carreau and Carreau-Yasuda models) and Newtonian blood flow viscosity using 9 patient specific coronary artery models including the full range of real stenosis. Results show that the wall shear stress varies along the artery. It increases with decreasing of artery cross sectional area. Newtonian and non-Newtonian models result in different WSS distributions, but behave similarly at the stenosis location. This indicates that the Newtonian model is acceptable in predicting WSS over the stenosis segment.
So, it is reasonable in our study to consider blood as a Newtonian fluid because:

- we are interested in the medium flow and not in the deeper details of the flow itself, therefore non-Newtonian behaviors can be neglected [3],

- we consider arteries with the radii of the order 5 mm, where the velocity and shear rate are not so small, therefore the apparent viscosity is nearly a constant, and the non-Newtonian effects like shear thinning can be neglected [5], [6].

In addition, we assume blood as an incompressible flow, like a lot of work in literature [3], [4], [5], [7], [8].
Mathematical details following these assumptions are given in the next section. Finally, for the sake of simplicity, the model is developed in an isothermal setting.

2.2 Navier-Stokes equations

The Navier-Stokes (N-S) equations are the fundamental equations of fluid dynamics. Georg Gabriel Stokes (1816–1903) and Louis Marie Henri Navier (1785–1836) derived these equations independently, so these equations take their names. Their complicated mathematical form mostly confines engineers to the numerical solution of these equations.

The mathematical proof of the existence of a global solution of the N-S equations is still one of the millennium problems [18].
In the case of an isothermal flow, N-S equations represent two physical conservation laws: the mass conservation and the momentum conservation.
In the following, we present only the local form of these models, even if it is not difficult to derive from the global form as presented in [19].

2.2.1 Mass conservation

Let us consider the motion of the blood in a time independent domain $\Omega \subset \mathbb{R}^3$ over a time interval of interest $(t_0, t^*]$, such that $\partial\Omega$ is smooth enough to apply the Gauss divergence theorem.
If $\rho = \rho(\mathbf{x}, t)$ is the density of the fluid and $\mathbf{u} = \mathbf{u}(\mathbf{x}, t)$ its velocity field, the mass conservation low is:

$$\frac{\partial \rho}{\partial t} + \nabla \cdot (\rho \mathbf{u}) = 0 \qquad \Omega \times (t_0, t^*]. \tag{2.1}$$

For the assumption of incompressible flow, the density is considered constant, so from 2.1 we obtain the velocity is a divergence-free vector:

$$\nabla \cdot \mathbf{u} = 0 \qquad \Omega \times (t_0, t^*]. \tag{2.2}$$

2.2.2 Momentum conservation

The local momentum conservation low is called Cauchy equation:

$$\frac{\partial}{\partial t}(\rho \mathbf{u}) + \nabla \cdot (\rho \mathbf{u}\mathbf{u}^T) = \mathbf{f} + \nabla \cdot \mathbb{T} \qquad \Omega \times (t_0, t^*], \tag{2.3}$$

where $\mathbf{f} = \mathbf{f}(\mathbf{x}, t)$ are the forces applied on the fluid and $\mathbb{T} = \mathbb{T}(\mathbf{x}, t)$ is a symmetric tensor, named stress tensor, which represents surface forces and it does not depend on surface normal.
For a Newtonian viscous fluid, it holds the constitutive relation 2.4:

$$\mathbb{T} = [-p + \lambda(\nabla \cdot \mathbf{u})]\mathbb{I} + 2\mu\mathbb{D}(\mathbf{u}), \tag{2.4}$$

where p is the hydrostatic pressure or simply pressure, μ is the dynamic coefficient of viscosity, λ is the second coefficient of viscosity [20] and $\mathbb{D}(\mathbf{u}) = \frac{\nabla \mathbf{u} + \nabla \mathbf{u}^T}{2}$ is a linear function of the components of the velocity gradient, named deformation tensor [1].
Since we have decided to consider blood as a Newtonian fluid, the viscosity μ is independent of any kinematic quantity. So, using 2.4 and 2.2, the local momentum conservation equation 2.3 is modified as follows:

$$\frac{\partial \mathbf{u}}{\partial t} + \nabla \cdot (\mathbf{u}\mathbf{u}^T) = \frac{\mathbf{f}}{\rho} - \nabla\left(\frac{p}{\rho}\right) + \nu \nabla \cdot (\nabla \mathbf{u} + \nabla \mathbf{u}^T) \qquad \Omega \times (t_0, t^*], \tag{2.5}$$

where $\nu = \frac{\mu}{\rho}$ is the kinematic viscosity.
It is possible to write:

$$\nabla \cdot (\mathbf{u}\mathbf{u}^T) = \nabla \cdot (\mathbf{u} \otimes \mathbf{u}) = (\mathbf{u} \cdot \nabla)\mathbf{u}, \tag{2.6}$$

and, using the incompressible constrain:

$$\nabla \cdot (\nabla \mathbf{u} + \nabla \mathbf{u}^T) = \Delta \mathbf{u} + \nabla(\nabla \cdot \mathbf{u}) = \Delta \mathbf{u}. \tag{2.7}$$

So, setting $P = \frac{p}{\rho}$ the pressure divided by the density (kinematic pressure) and $\mathbf{F} = \frac{\mathbf{f}}{\rho}$ the forces per unit of mass, we obtain a compact form for incompressible N-S equations:

$$\begin{cases} \frac{\partial \mathbf{u}}{\partial t} + (\mathbf{u} \cdot \nabla)\mathbf{u} - \nu \Delta \mathbf{u} + \nabla P = \mathbf{F} & \Omega \times (t_0, t^*] \\ \nabla \cdot \mathbf{u} = 0 & \Omega \times (t_0, t^*] \end{cases}, \tag{2.8}$$

where $\frac{\partial \mathbf{u}}{\partial t}$ is the eulerian acceleration of the fluid, $\Delta \mathbf{u}$ represents the molecular diffusion process and $(\mathbf{u} \cdot \nabla)\mathbf{u}$ is a non linear term which describes the convective transport process. For the good position of the problem 2.8, it is necessary to assign initial conditions:

$$\mathbf{u}(\mathbf{x}, 0) = \mathbf{u}_0(\mathbf{x}) \qquad \forall \mathbf{x} \in \Omega, \tag{2.9}$$

and boundary conditions:

$$\begin{cases} \mathbf{u}(\mathbf{x}, t) = \phi(\mathbf{x}, t) & \forall \mathbf{x} \in \Gamma_D, \forall t \in (t_0, t^*] \\ [\nu(\nabla \mathbf{u} + \nabla \mathbf{u}^T)\mathbf{n} - P\mathbf{n}](\mathbf{x}, t) = \psi(\mathbf{x}, t) & \forall \mathbf{x} \in \Gamma_N, \forall t \in (t_0, t^*] \end{cases}, \tag{2.10}$$

where $\mathbf{u}_0$, ϕ and ψ are assigned vector functions, Γ_D and Γ_N are parts of $\partial\Omega$ such that $\Gamma_D \cup \Gamma_N = \partial\Omega$ and $\overset{\circ}{\Gamma}_D \cap \overset{\circ}{\Gamma}_N = \emptyset$, finally $\mathbf{n}$ is the normal unit vector to $\partial\Omega$ [21].

2.3 Boundary conditions

Boundary conditions are essential in order to obtain meaningful cardiovascular simulation results. It is fundamental that boundary conditions capture as much as possible the physiology of vascular networks outside of the domain of the model. For this reason, in the present work, we opted for boundary conditions based on realistic flow rate waveform. In our geometry, we have:

- inflow boundaries: for LMCA and LITA,
- vessel wall boundary: the interface between the fluid domain and the vessel wall,
- outflow boundaries: for LAD and LCx.

For inflow boundaries, we will prescribe a zero gradient condition for the pressure and a flow wave profile obtained from literature. The flow rate at each inlet of the computational model is expressed as:

$$q_i(t) = f^i \bar{q}_i(t) \qquad i = LMCA, LITA. \tag{2.11}$$

Some points of the function $\bar{q}_i(t)$ are taken from [8] thanks to *engauge digitizer*. Then a linear combination of sines and cosines so that the period is equal to the cardiac cycle ($0.8s$) is used to fit the data points extracted. It is performed using the class OLS (ordinary

least squares) of the python module *statsmodels*. Functions obtained and data points extracted for LMCA and LITA are shown in Figure 2.1.
The multiplicative factor f^i is computed from [52], [53] and [54]. In particular for LITA the average flow of [53] and of the Figure 2.1 are compared to find $f_{LITA} \simeq 0.82$. For LMCA the comparison of diastolic velocity peak in [52] and in the Figure 2.1 gives $f_{LMCA} \simeq 1.12$. For the last calculation the average area of the LMCA section is necessary because in [52] there is the diastolic peak of the velocity while in Figure 2.1 the flow is plotted. This data is provided by [54].

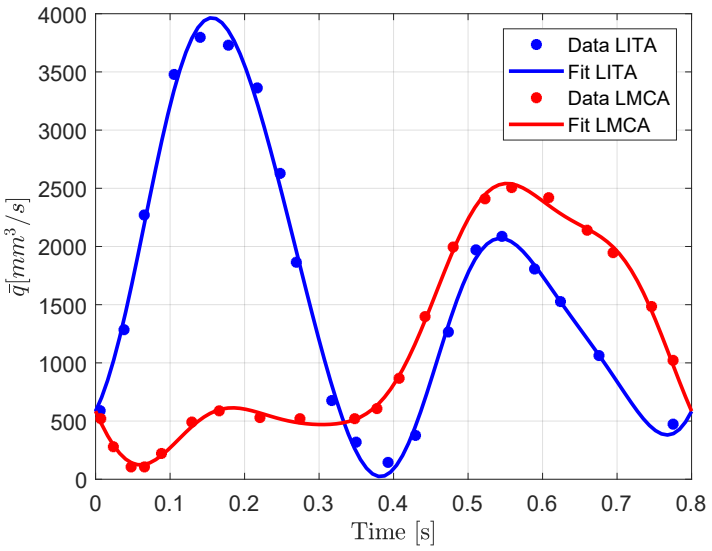

Figure 2.1: Boundary conditions of the LMCA and LITA.

For the vessel wall boundary, traditionally it is used a rigid wall assumption, in which a zero velocity condition is applied on this surface, the so called no slip condition. For the pressure a zero gradient condition is used because this condition simply extrapolates the quantity from the nearest cell value.
Finally, for the outflow boundaries, it is prescribed a pressure value that is uniform over the face (spatially constant) and a zero gradient velocity condition. It is interesting to observe that, since we are not interested in the exact pressure value for an incompressible flow in a channel, but only pressure differences, we would set the pressure to be 0 at the outlet and zero gradient on the inlet.
Since stenosis changes the inlet flow and it will be considered more than one stenosis degree, it is relevant to scale flow rates at each inlet as:

$$\bar{Q}^{healthy}_{LMCA} = \bar{Q}^{stenosis}_{LMCA} + \bar{Q}^{stenosis}_{LITA} = G\bar{Q}^{healthy}_{LMCA} + C\bar{Q}^{healthy}_{LITA}, \tag{2.12}$$

where $\bar{Q}_i = \frac{1}{T}\int_0^T f^i \bar{q}_i(t)\,dt$ with $i = LMCA, LITA$, G is related to the degree of the stenosis and C is the parameter used to scale the boundary condition of the LITA.

Chapter 3

Numerical discretization

In the current chapter, we discuss the discretization method used in our work, the finite volume method (FVM). It is a discretization procedure applied to solve numerically differential equations. Similar to other numerical methods used for fluid dynamic simulations, the FVM transforms the set of partial differential equations under consideration into a system of linear algebraic equations. The basic step for FVM is the discretization of the domain, so in the following we will analyse also some problems related to this topic.

3.1 Finite volume method

FVM is a discretization technique used especially for physical conservation laws, as N-S equations. The numerical procedure developed involves two basic steps. In the first step, the domain is discretized into non-overlapping finite volumes, named control volumes. The partial differential equations are then transformed into algebraic equations by integrating them over each discrete element. In the second step, interpolation profiles are chosen in order to approximate the variation of the variables in each element and relate the surface values of the variables to their cell values.
Because the flux entering a given volume is identical to that leaving the adjacent volume, the FVM is conservative. This property of the FVM makes it the favourite method in CFD [30]. As [33] and [34], we decided to use this approach for our study on coronaries. This choice is supported also by [32], where a validation of numerical solutions of the entire coronary artery model was performed.
Let us consider a decomposition of Ω in control volumes V_j and a time step $\Delta t > 0$ such that $t_n = n\Delta t$, $n = 0,1,\ldots$.
Equation 2.8 can be written using the divergence theorem as follow:

$$\frac{\partial}{\partial t}\int_{V_j} \mathbf{u} d\Omega + \int_{\partial V_j} (\mathbf{u}\otimes\mathbf{u})\cdot d\mathbf{A} - \nu\int_{\partial V_j} \nabla\mathbf{u}\cdot d\mathbf{A} + \int_{V_j}\nabla P d\Omega = \int_{V_j}\mathbf{F} d\Omega. \tag{3.1}$$

Each term is examined in detail.
If $\mathbf{A}_f$ is the surface vector of each face f of the control volume, the discretization of the

convection term brings to:

$$\int_{\partial V_j} (\mathbf{u} \otimes \mathbf{u}) \cdot d\mathbf{A} \simeq \sum_f (\mathbf{u}_f \otimes \mathbf{u}_f) \cdot \mathbf{A}_f = \sum_f (\mathbf{u}_f \cdot \mathbf{A}_f)\mathbf{u}_f, \tag{3.2}$$

where $\mathbf{u}_f \cdot \mathbf{A}_f$ is the convective flux associated to $\mathbf{u}$ through face f of the control volume and $\mathbf{u}_f$ is the fluid velocity relative to the centroid of each control volume face. Different interpolation methods can be used to compute the value of the convective flux and the velocity at the face f; we will use the convection linear upwind difference scheme. Consider P local control volume central point and N neighbour control volume central point as in Figure 3.1. The value of a physical quantity ϕ_f under consideration changes according to the direction of the flow as follows:

$$\phi_f = \begin{cases} \frac{3\phi_N - \phi_P}{2} & \mathbf{u}_f < 0 \\ \frac{3\phi_P - \phi_N}{2} & \mathbf{u}_f > 0 \end{cases}. \tag{3.3}$$

Similarly, the diffusion therm can be discretized as:

$$\int_{\partial V_j} \nabla \mathbf{u} \cdot d\mathbf{A} \simeq \sum_f (\nabla \mathbf{u})_f \cdot \mathbf{A}_f. \tag{3.4}$$

In the case of mesh orthogonality, i.e. vectors $\mathbf{d}_f$ and $\mathbf{A}_f$ in Figure 3.1 are parallel, it can be treated as follow:

$$(\nabla \mathbf{u})_f \cdot \mathbf{A}_f = \frac{\mathbf{u}_N - \mathbf{u}_P}{\mathbf{d}_f} |\mathbf{A}_f|, \tag{3.5}$$

where $\mathbf{d}_f$ is the distance between P and N.
For non-orthogonal meshes, a correction term may be necessary:

$$(\nabla \mathbf{u})_f \cdot \mathbf{A}_f = \underbrace{(\nabla \mathbf{u})_f \cdot \mathbf{\Delta}_f}_{\text{ortogonal contribution}} + \underbrace{(\nabla \mathbf{u})_f \cdot \mathbf{k}_f}_{\text{non ortogonal correction}}, \tag{3.6}$$

where vectors $\mathbf{\Delta}_f$ and $\mathbf{k}_f$ in Figure 3.1 satisfy:

$$\mathbf{A}_f = \mathbf{\Delta}_f + \mathbf{k}_f. \tag{3.7}$$

Many possible decompositions exist and a detailed explanation can be found in [31].
So far, we have analysed surface terms. For volume terms we can use indifferently the cell centre value or the cell mean value. It is possible because we use second order methods and the difference between the cell centre value and the cell mean value is of higher order. For the pressure term, if P is the centroid of the control volume under consideration and N a cluster of points around it, it is possible to write:

$$\int_{V_j} \nabla P d\Omega = (\nabla P)_P |V_j|. \tag{3.8}$$

In order to estimate the pressure gradient, we use the least square method. If we consider the plane:

$$e_N = P_N - (P_P + \mathbf{d}_f \cdot (\nabla P)_P), \tag{3.9}$$

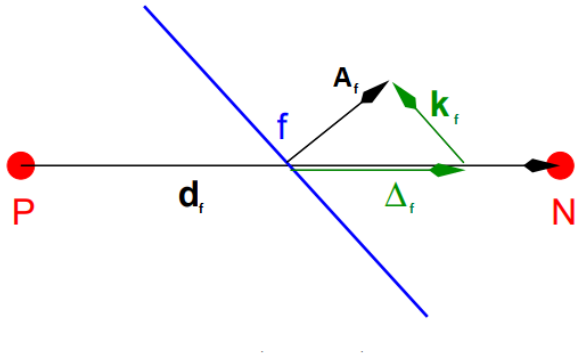

Figure 3.1: Non-orthogonal mesh.

this method want to minimize the weighted error:

$$e_P^2 = \sum_N (w_N e_N)^2, \quad \text{where} \quad w_N = \frac{1}{|\mathbf{d}_f|}. \tag{3.10}$$

This yields to the following form of the gradient:

$$(\nabla P)_P = \sum_N w_N^2 G^{-1} \cdot \mathbf{d}_f (P_N - P_P), \quad \text{where} \quad G = \sum_N w_N^2 \mathbf{d}_f \mathbf{d}_f. \tag{3.11}$$

For the source term, as before we can write simply:

$$\int_{V_j} \mathbf{F} d\Omega = \mathbf{F}_P |V_j|. \tag{3.12}$$

Finally if:

$$\int_{V_j} \mathbf{u} d\Omega = \mathbf{u}_P |V_j|, \tag{3.13}$$

using a backward differencing scheme, the temporal derivative is calculated:

$$\frac{\partial \mathbf{u}_P}{\partial t} = \frac{1}{\Delta t}\Big(\frac{3}{2}\mathbf{u}_P^n - 2\mathbf{u}_P^0 + \frac{1}{2}\mathbf{u}_P^{00}\Big), \tag{3.14}$$

where $\mathbf{u}_P^n = \mathbf{u}_P(t + \Delta t)$, $\mathbf{u}_P^0 = \mathbf{u}_P(t)$ and $\mathbf{u}_P^{00} = \mathbf{u}_P(t - \Delta t)$.
To solve the Navier-Stokes equations we need to use a solution approach able to deal with the coupled set of equations. Many numerical methods exist, we use a segregated pressure-correction method. The velocity field is obtained from the momentum equation and the individual governing equations for the primitive variables are solved one after another.
The PISO and PIMPLE methods are available in OpenFOAM®for unsteady simulations.

The PISO (Pressure-Implicit with Splitting of Operators) algorithm, chosen for this work, consist of three steps briefly mentioned:

- Predictor step: the pressure field at the previous step t_n is used in the solution of the implicit momentum equation to yield the u^* velocity field. It should be noted that in general it does not satisfy the zero-divergence condition.
- First corrector step: A new velocity field, u^{**} together with a corresponding new pressure field, p^*, is now sought such that the zero-divergence condition is met. In this step a Poisson equation for the pressure is derived applying the divergence to the momentum equation and using the zero-divergence condition. The p^* field obtained is inserted in the explicit momentum equation yielding u^{**}.
- Second corrector step: A new velocity field, u^{***} together with a corresponding new pressure field, p^{**}, is now sought as before.

It can be shown that two corrector steps are a good number in order to obtain velocity and pressure fields that approximate the exact solution well enough.
Actually, for accuracy and stability reasons, the method presents some modifications not analysed here. Details are discussed in [35].

3.2 Domain discretization

The generation of the mesh is the first step to solve numerically N-S equations. It is fundamental to build a good quality mesh in order to obtain meaningful results.
If the goal is to discretize a complex domain as coronary arteries, inevitably some of the following errors are made:

- errors due to grid gradient, it is caused by different characteristic lengths of consecutive cells (Figure 3.2c),
- errors due to non orthogonality of the mesh, caused by the angle between the line joining the nodes of two adjacent control volumes and the face intersected it (Figure 3.2b),
- errors due to obliquity, caused by the distance between the midpoint of the face and the intersection point between the junction of the nodes of adjacent cells and the face (Figure 3.2a).

In our simulations, the mesh is built by step in order to limit previous errors:

- around the geometry we generate a parallelepiped discretized with squared cells;
- intersection between the external block and the geometry is performed in order to maintain only cells in the internal region of the coronary;
- finally, castellation and snapping are carried out in order to obtain a more realistic boundary.

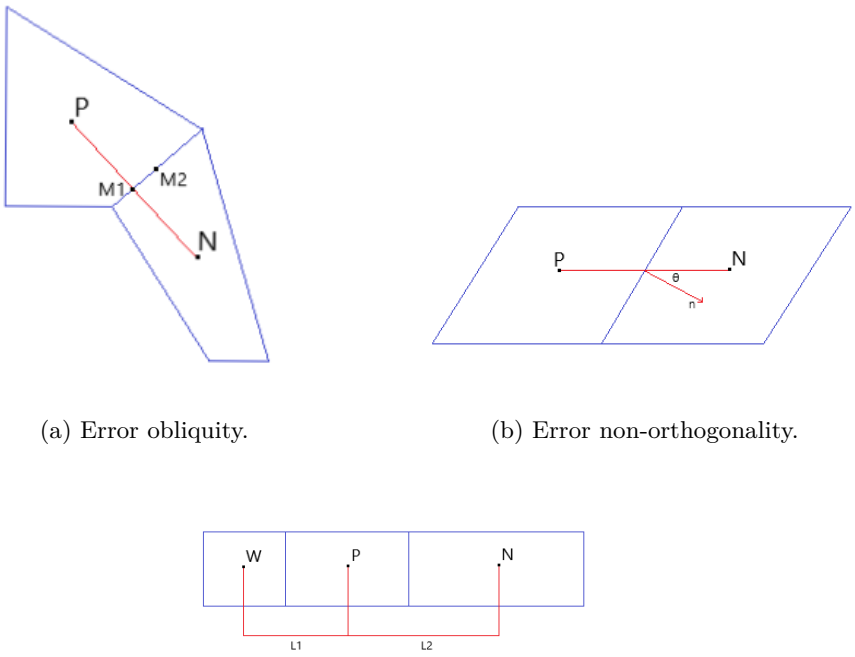

(a) Error obliquity.

(b) Error non-orthogonality.

(c) Error grid gradient.

Figure 3.2: Errors due to grid.

In addition, it could be possible to switch on surface layer insertion. The Reynolds number in the coronary system is small when compared to larger arteries like carotid and aorta due to reduced blood flow rate and diameter of the coronary arteries, so the surface layer insertion could not be necessary in our application (remember the inverse proportionality between Reynolds number and boundary layer thickness). However in order to obtain meaningful results in term of WSS we decided to introduce the boundary layer. This is advisable when dealing with hemodynamics because the solution near the wall, in particular the wall velocity gradient, is rather important as it is used to compute the wall shear stress. By the way, this allows to observe that the flow is generally assumed to be laminar for coronary arteries like LMCA, LCx, LAD and RCA [37], so turbulence models are not required.
Actually, some studies as [37], [38] and [39] show that blood flow through coronary arteries under stenotic condition could result in transition from laminar to turbulent flow. In particular, blood flow in stenotic coronary arteries can be turbulent in nature for area stenosis above 70% and the transition to turbulent flow starts from 50% stenosis. The reason is simply that in the region of the stenosis the velocity increases and the radius decreases, so that the flow is still laminar, but in the region downstream of the stenosis, whilst the velocity is still high by inertia, the increase of the radius causes turbulence.

This aspect cannot be neglected because, even if in a stenosis the pressure drop is well predicted without introducing a turbulence model [39], WSS calculated using turbulence model deviates from laminar by more than 10% and as the turbulence level in the blood flow rises the value of the WSS increases due to growth in the velocity gradient at the wall [37].
However, our aim is to avoid introducing turbulence models solving the motion field in all its parts appropriately refining the mesh and doing a mesh convergence analysis, basically performing a DNS (Direct Numerical Simulation).

3.3 Geometry

Due to covid emergency, Sacco hospital in Milan could not provide us a new geometry. So, we decided to use an old domain of Francesco Ballarin's doctoral thesis [36] opportunely modified. Using VMTK and Meshmixer in order to close the boundary and to remove additional branches, we obtained the configurations for CABG1 and CABG2 respectively shown in Figure 3.3a and 3.3b. Only two slight differences can be seen with respect to the configurations in the Figure 1.2a and 1.2b. In fact, the bypass is performed with the SV from the LITA instead of with the RITA from the subclavian artery. It is necessary in order to avoid the introduction of an additional boundary condition for the RITA, which would have been unrealistic due to the lack of studies. Furthermore, the bypass does not end directly on the LCx, but on a subsequent branch. This is due to the initial geometry, however it does not lead to substantial differences.

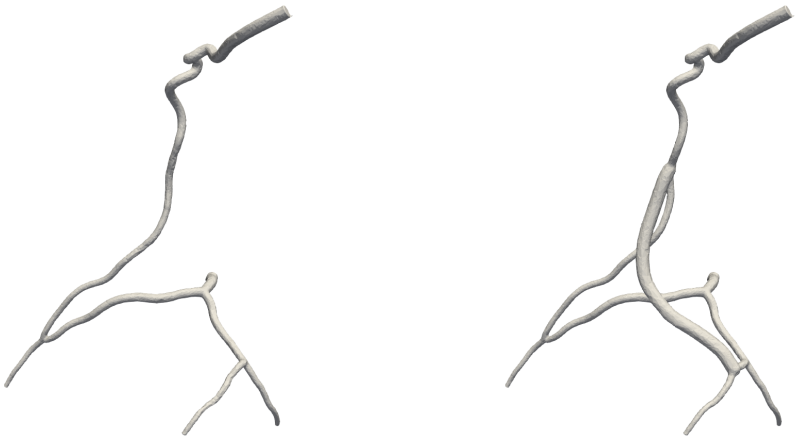

(a) CABG1. (b) CABG2.

Figure 3.3: Configurations.

3.3.1 Mesh convergence

Mesh convergence identifies how many elements are needed in a model to ensure that the results of an analysis are not influenced by the size of the mesh. After convergence is achieved, extra mesh refinement does not impact the results. By this time the model and its results are independent of the mesh. A mesh convergence study ensures that the FVM model converges to a solution. It also gives a justification for mesh independence and clarifies when additional refinement is unnecessary.
The geometry chosen for this analysis is CABG1 without stenosis and features of the grids used for the study are shown in Table 3.1. In Figure 3.4 are shown the mean pressure and

	Cells number	Min-max volume $[mm^3]$	Non-orthogonality	Max skewness
Mesh1	518.299	8.5e-14 - 1.9e-10	13.2	2.50
Mesh2	986.278	2.8e-14 - 8.0e-11	12.9	2.95
Mesh3	1.829.291	1.2e-14 - 2.5e-10	12.7	2.60

Table 3.1: Features of the grids.

velocity over time for the three meshes. To be clear, mean pressure and mean velocity are:

$$\bar{p} = \frac{1}{\Omega} \int_{\Omega} p d\Omega,$$

$$\bar{U} = \frac{1}{\Omega} \int_{\Omega} U d\Omega.$$

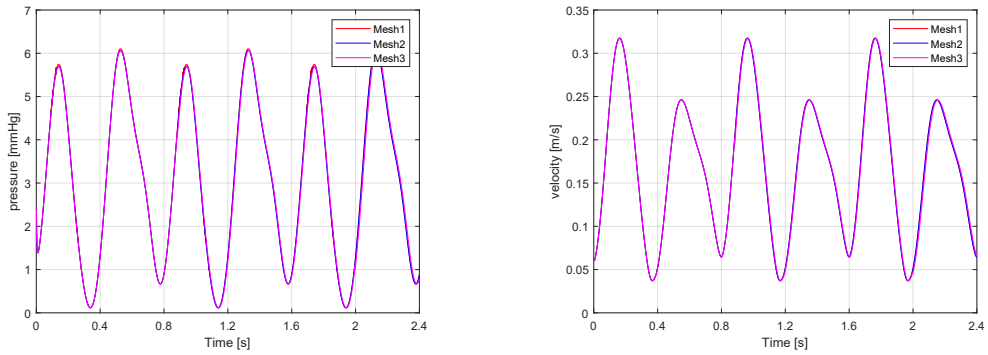

Figure 3.4: Mean pressure and velocity over time.

It is possible to observe how the simulation reaches the steady state already from the first cardiac cycle. Moreover, qualitatively it is clear that results are good for all meshes, because the graphs are totally overlapping.

Quantitatively, we can compute the relative error:

$$\epsilon = \frac{1}{n}\sum_{i=1}^{n}\frac{|x_{ij} - x_{i3}|}{\hat{x}_{i3}}, \quad with \quad j = 1{,}2 \quad and \quad x = \bar{p}, \bar{U},$$

where n is the number of time steps, the subscript 3 (and j) indicates the quantity of Mesh3 (and Mesh1, Mesh2) and $\hat{x}_{i3}$ is the mean of x_3. Results are shown in Table 3.2.

Finally, thanks to the introduction of the boundary layer, it is possible to obtain meaningful results also in terms of WSS. If the stress tensor is:

	Mesh1	Mesh2
$\epsilon_p(\%)$	0.73	0.15
$\epsilon_U(\%)$	0.23	0.047

Table 3.2: Relative errors due to grid.

$$\tau = \nu(\nabla \mathbf{u} + \nabla \mathbf{u}^T), \tag{3.15}$$

WSS is defined as:

$$WSS = \tau \cdot \mathbf{n}, \tag{3.16}$$

where $\mathbf{n}$ is the unit normal vector.
In Figure 3.5 can be found the point value of WSS for the three meshes at the bifurcation point at $1.8s$ and similar results are observed for the other time steps.
For all simulations of the work, we will use Mesh2 and the Reynolds number $Re = \frac{UL}{\nu}$ is about 100.

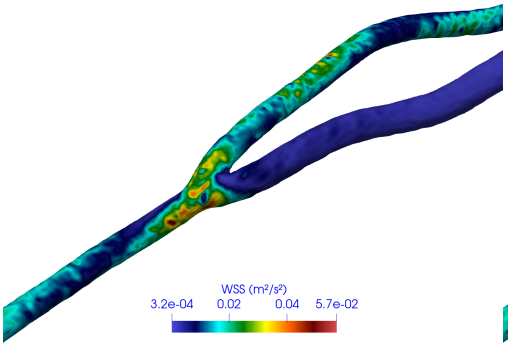

(a) WSS Mesh1.

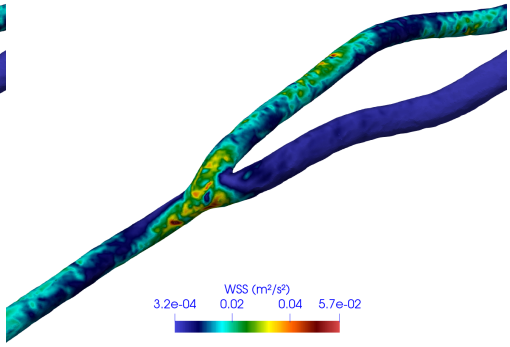

(b) WSS Mesh2.

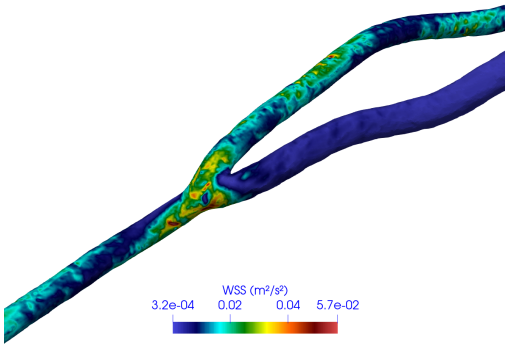

(c) WSS Mesh3.

Figure 3.5: WSS convergence.

Chapter 4

Reduced order method

High-fidelity numerical methods are very used in applications with parametrized partial differential equations, where the parameters are geometric features, boundary conditions and physical properties [40]. This is exactly our case because the problem under examination 2.8 applied to the coronary geometry depends on the parameter $\mu \in \mathbb{P}$ such as the time, the degree of the stenosis or the inlet flow.
For applications which require repeated model evaluations over a range of parameter values, high-fidelity simulations remain expensive in terms of CPU time and memory demand due to the large amount of degrees of freedom N_h. The need of cost reduction in such applications has led to the development of reduced-order modeling (ROM) that wants to build low-dimensional models fast and cheap to evaluate but providing accurate predictions [41]. The aim of these methods is to replace the full-order system by one of substantial smaller dimension, to decrease the computational cost while leading to a controlled loss of accuracy.
Reduced basis (RB) methods represent a well-known and widely-used example of reduced order modeling techniques [42]. The final goal of RB methods is to approximate any member of the solution manifold with a low number of basis functions. This set of basis functions is denoted as the reduced basis [43]. RB methods consist of two stages:

- offline: computationally it is the most expensive step, however it only needs to be performed once. The goal of this phase is the construction of a reduced base for the problem through the POD algorithm.

- online: it can be performed in an environment that has limited computational power and memory. It consists of a projection of the problem onto the space spanned by the reduced basis. During this stage, it is possible to explore the parameter space at a significantly reduced cost.

Actually, operations performed during these stages are a little different for each RB method chosen.
The reader is referred, e.g, to [9], [10], [11], [12], [13], [14], [15], [16] and [17] for a complete review about the state of the art. In this work, we decided to implement POD-NN method (Proper Orthogonal Decomposition-Neural Network), so at the offline stage also

the training of a network to find the coefficients of the reduced solution is carried out. Due to the development and diffusion of intelligent technologies with increasing impact for human beings [44], we decided to apply a RB method based on machine learning. It is relevant to note that, to our knowledge, it is the first time that POD-NN method has been applied in the case of coronary arteries.
We decided to implement this method for some reasons clarified in the following.
In particular, in [55] it is developed a machine learning approach that demonstrates the possibility of using machine learning as a fast and accurate alternative to CFD in order to estimate steady state hemodynamic fields of the human thoracic aorta. In this approach, CFD is seen as a black box, and the machine learning algorithm learns the nonlinear link between CFD input and output. So, it appears that machine learning models can be an appetizing alternative to CFD simulations to support clinical decisions and treatments for specific patients. It is also argued by [56], where it is proposed a deep learning approach to estimate the time average wall shear stress (TAWSS), an hemodynamic risk indicator, based on the vessel geometry. The neural network model predicts TAWSS on left main coronary artery with a 10.4% deviation from the real value. Concerning WSS, also [58] aims to use machine learning as an alternative to CFD. The goal is to produce hemodynamic parameters in real-time diagnosis during medical examinations. As in previous papers, CFD is used to compute the data set for training and testing. They have explored multivariate linear regression, multi-layer perceptron and convolutional neural network architectures. With good results, they were able to produce WSS values from coronary artery geometry directly without CFD.
Others works employ neural network architectures as physics-informed neural networks (PINN). For example [57] uses it to solve the forward and inverse problems for the one-dimensional and two-dimensional Euler equations. In this case, the architecture of PINN contains two NNs sharing hyper-parameters and both contributing to the loss function, one is the uninformed NN associated with the data while the other is the informed one associated with the conservation laws. In [59], PINN is proposed to estimate flow variables as blood velocity, wall displacement and pressure in a given arterial network. Actually, this method is used with success also in areas totally different such as molecular dynamics [60]. Therefore, all these studies have brought us closer to artificial intelligence, in particular our attention has focused on the artificial neural network method.
Anyway, more classical methods can coexist in harmony with deep neural networks. Our aim is to come up with a partnership between machine learning and more classical computational methods that has the potential to enrich both fields. So, fueled by this ambition, we analysed two papers [40] and [42]. There, a good performance is found in the combination of reduced models and neural networks. In particular POD-NN method is applied in [42] for the Poisson equation and the two-dimensional incompressible steady Navier-Stokes equations and POD-PINN in [40] for the Burger's equation, lid-driven cavity flow problem and natural convection.
Therefore, the presented bibliographic research prompted us to try to apply and extend POD-NN method also in the hemodynamic field. Actually, in the future we would like to try to use the POD-PINN method as well.

4.1 Proper orthogonal decomposition (POD)

To begin, let's clarify some notations. So far, we have not specified that the solution of the problem depends on some parameters $\mu \in \mathbb{P}$, but hereinafter it is crucial. The exact solution $\mathbf{u} = \mathbf{u}(\mu)$ of 2.8 is not available in an analytic way. This is why FVM is required. From now on, $\mathbf{u_h}(\mu)$ is the solution obtained with the FVM and it is called truth solution. We assume that the distance between $\mathbf{u}(\mu)$ and $\mathbf{u_h}(\mu)$ can be made arbitrarily small for any given parameter value $\mu \in \mathbb{P}$, substantially we assume that with the FVM we can solve the truth problem at any required accuracy. However, we will not specify the details of this topic because it goes beyond the purpose of the project. At this point we can define the solution manifolds [43]:

$$\mathbb{M} = \{\mathbf{u}(\mu), \mu \in \mathbb{P}\}, \tag{4.1}$$

and

$$\mathbb{M}_h = \{\mathbf{u_h}(\mu), \mu \in \mathbb{P}\}. \tag{4.2}$$

There are two major techniques to generate the reduced space: POD and greedy algorithm. With the last, the basis vectors coincide with the snapshots (i.e., high fidelity solutions of the parametrized differential problem) themselves, carefully selected. Greedy strategy is typically more effective and efficient than POD because fewer high-fidelity solutions are computed [42]. However, we will use the POD method because there exist problems for which a greedy approach is not viable, simply because a natural criterion for the choice of the snapshots is not available (more details about the failure of the greedy algorithm are present in [45]).
Let us introduce a discrete and finite-dimensional point-set $\mathbb{P}_h = \{\mu_1, \dots, \mu_N\} \subset \mathbb{P}$ in the parameter domain generated by either a uniform lattice or randomly generated points. It is possible to introduce a collection of N snapshots $\{\mathbf{u}_h(\mu_1), \dots, \mathbf{u}_h(\mu_N)\}$ and :

$$\mathbb{M}_{\{\mu_1,\dots,\mu_N\}} = span\{\mathbf{u}_h(\mu_1), \dots, \mathbf{u}_h(\mu_N)\}. \tag{4.3}$$

We assume that $\mathbb{M}_{\{\mu_1,\dots,\mu_N\}}$ is good enough to represent $\mathbb{M}_h$ if the number of snapshots is sufficiently large.
Operatively, consider the snapshots matrix:

$$\mathbb{S} = \{\mathbf{u}_h(\mu_1)|\dots|\mathbf{u}_h(\mu_N)\} \quad N_h \times N. \tag{4.4}$$

Usually, this matrix is not square, and, denoting by $R \leq min(N_h, N)$ its rank, the singular value decomposition (SVD) allows to factorise $\mathbb{S}$ as:

$$\mathbb{S} = \mathbb{W}\mathbb{D}\mathbb{Z}^T, \tag{4.5}$$

where $\mathbb{W} = \{\mathbf{w}_1|\dots|\mathbf{w}_{N_h}\}$ $N_h \times N_h$ and $\mathbb{Z} = \{\mathbf{z}_1|\dots|\mathbf{z}_N\}$ $N \times N$ are two orthogonal matrices composed of left singular vectors and right singular vectors respectively in columns, and $\mathbb{D}$ $N_h \times N$ is a diagonal matrix with R non-zero singular values $\sigma_1 \geq \sigma_2 \geq \dots \geq \sigma_R > 0$.
At the algebraic level, our goal is to approximate the columns of $\mathbb{S}$ by means of $L < R$

orthonormal vectors. The Schmidt-Eckart-Young theorem states that the POD basis of rank L consists of the first L left singular vectors of $\mathbb{S}$, $\{\mathbf{w}_1, \dots \mathbf{w}_L\}$ [46]. So we can introduce the matrix:

$$\mathbb{V} = \{\mathbf{w}_1 | \dots | \mathbf{w}_L\} \quad N_h \times N, \tag{4.6}$$

and the reduced space:

$$\mathbb{V}_{rb} = span\{\mathbf{w}_1, \dots, \mathbf{w}_L\}. \tag{4.7}$$

From a more theoretical point of view, it is interesting to note that the POD basis of size L is the solution to the minimization problem:

$$\min_{V} \|\mathbb{S} - \mathbb{V}\mathbb{V}^T\mathbb{S}\| \quad s.t. \quad \mathbb{V}^T\mathbb{V} = \mathbb{I}, \tag{4.8}$$

where $\| \bullet \|$ is the Frobenius norm or the Euclidian norm.
Substantially we are looking for the basis that minimizes the distance between the snapshots and their projection into the space spanned by the basis. In addition, the error in the POD basis is equal to the sum of the squares of the neglected singular values, i.e., by controlling the size L, we can approximate the snapshots matrix $\mathbb{S}$ with arbitrary accuracy. Many problems exhibit an exponential decay of the singular values, allowing the use of a low-dimensional reduced space to approximate the high-fidelity solution with adequate accuracy [40]. So, essentially, in order to choose L, we will plot the singular values as function of N.
Finally, another interesting observation is the parallelism with the principal component analysis (PCA). In order to recognize the link between PCA and SVD we calculate the following matrix:

$$\mathbb{C} = \mathbb{S}\mathbb{S}^T = \mathbb{W}\mathbb{D}\mathbb{Z}^T\mathbb{Z}\mathbb{D}\mathbb{W}^T = \mathbb{W}\mathbb{D}^2\mathbb{W}^T, \tag{4.9}$$

that we can interpret as a covariance matrix. It suggests that the square roots of the eigenvalues of $\mathbb{C}$ are the singular values of $\mathbb{S}$ and the left eigenvectors of $\mathbb{S}$ represent the vectors pointing in the direction that maximizes the variance [47].
POD method is implemented entirely offline, because it is expensive and it needs to be performed only once.

4.2 Artificial neural network (ANN)

Artificial neural network (ANN) or simply neural network (NN) is a computational model able to learn from observational data. It consists of neurons and a set of directed weighted synaptic connections among the neurons. Substantially, it is an oriented graph, with the neurons as nodes and the synapses as oriented edges, whose weights are adjusted by means of a training process to configure the network for a specific application. Let us consider the neuron j and suppose that it is connected with m sending neurons $\{s_1, \dots s_m\}$ and n receiving neurons $\{r_1, \dots r_n\}$. Neuron j gets the weighted inputs $w_{s_k,j}y_{s_k}(t)$ and send out the output $y_j(t + \Delta t)$. To understand better, a scheme is reported in Figure 4.1.
Three functions characterize completely the neuron j:

- the propagation function: it converts the input $\{s_1, \dots, s_m\}$ into a scalar $u_j = \sum_{k=1}^{m} w_{s_k,j}y_{s_k}$, so it is used to transport values through the neurons of an ANN. A common choice is the weighted sum, but also non linear choices are possible.

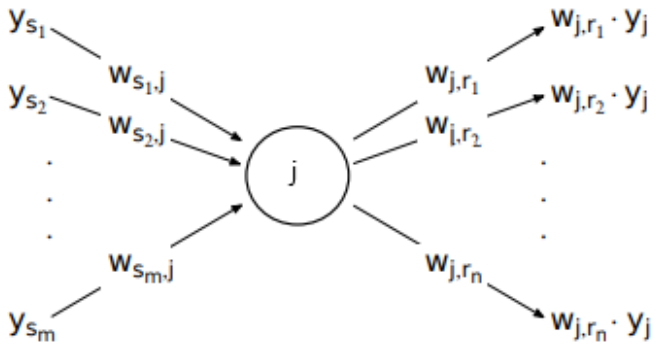

Figure 4.1: Scheme of a neuron.

- the activation function: it quantifies to which degree neuron j is active. It is a function of the input u_j and a threshold parameter θ_j chosen during the training process. Operatively the neuron threshold is set to zero and θ_j is treated as a synaptic weight $w_{b,j} = -\theta_j$ with output $y_b = 1$. The most commonly used activation functions are non-linear activation functions, because if a linear function is used, the network can adapt to only the linear changes of the input, but real world possesses non-linear characteristics. Commonly used functions are sigmoid function, hyperbolic tangent, RELU, SoftMax. More details can be found in [48].

- the output function: it calculates the scalar output y_j based on the activation state a_j of the neuron. Often it is the identity function, so that activation and output of a neuron coincide.

The interconnection of neurons within a network defines the topology of the network [42]. A feedforward network, also called perceptron, is one whoso topology has no closed paths and often it is used for function regression tasks. The input nodes are the ones with no arcs to them, and the output nodes have no arcs away from them. All other nodes are hidden nodes. In a feedforward neural network, neurons are arranged into layers, so input nodes define one input layer and the same holds for the output layer and for the hidden layers. Neurons in a layer can only be linked with neurons in the next layer, towards the output layer. When an input vector is supplied, a feedforward network establishes a map between the input space and the output space. A network is fully connected if each node in layer I is connected to all nodes in layer $I + 1$ for all I.
Layered feedforward networks have become very popular firstly because they have been found in practice to generalize well. Secondly, a training algorithm called backpropagation exists which can often find a good set of weights (and biases) in a reasonable amount of tune. Backpropagation is a variation on gradient search. The procedure repeatedly changes the weights of the connections in the network in order to minimize the difference between the actual output vector of the net and the required output vector. It generally uses a least-squares optimality criterion. The key to backpropagation is a method

for computing the gradient of the error with respect to the weights for a given input by propagating error backwards through the network. For a complete discussion of the backpropagation we refer to [50]. A loss function is introduced to optimize the parameter values in a neural network model. This class of functions maps a set of parameter values for the network onto a scalar value that shows how well those parameters achieve the purpose the network is intended to do. Different loss functions can be employed according to the problem under examination.
Feedforward networks can be classified depending on the number of hidden layers. Multilayer neural network with two hidden layers and differentiable activation functions can approximate any function [49], for this reason we will use a network similar to Figure 4.2. In addition to the parameters already mentioned, also the number of neurons in the hidden layers is decided during the learning process. Hence, given an initial amount of training samples N_{tr}, we train the network for increasing values of hidden neurons H, stopping when overfitting of training data occurs, due to an excessive number of neurons. Naturally, because it needs to be done only once, the training step in order to find an optimal network configuration is implemented offline.

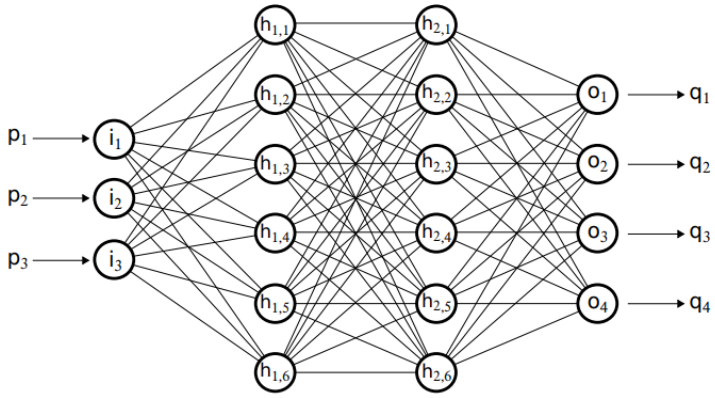

Figure 4.2: Topology of the network.

In our case, the reduced coefficients are calculated by a neural network. The ANN seeks to minimize the mean squared error on sampled training points in parameter space. So labeled data are needed for the training. The loss function of the network becomes the sum of the mean squared errors between the network output and the labels.
In order to understand better where the ANN introduced before is used, it is necessary to make some observations. Once the reduced basis is available, we can write an element of $\mathbf{V}_{rb}$ as a combination of the basis functions:

$$\mathbf{v}_{rb} = \mathbb{V}\alpha = \sum_{j=1}^{L} \mathbf{v}_{rb}^{j} \mathbf{w}_j = \sum_{j=1}^{L} \mathbf{v}_{rb}^{j} \sum_{i=1}^{N_h} \mathbb{V}_{i,j} \phi_i = \sum_{i=1}^{N_h} (\mathbb{V}\mathbf{v}_{rb})_i \phi_i, \tag{4.10}$$

where α is a vector of coefficients to be found and $\{\phi_1, \ldots, \phi_{N_h}\}$ is a basis of $\mathbb{V}_h$.

The projection of $\mathbf{u}_h$ into $\mathbb{V}_{rb}$ algebraically corresponds to the projection of $\mathbf{u}_h$ into $col(\mathbb{V})$ (the space generated by the columns of $\mathbb{V}$), and this projection is the element of $col(\mathbb{V})$ closest to $\mathbf{u}_h$ in the Euclidian norm. Aware that $\mathbb{V}\mathbb{V}^T$ is the projection matrix (in fact it can be written as $\mathbb{V}\mathbb{V}^T = \sum_i \langle \mathbf{w}_i, \cdot \rangle \mathbf{w}_i$), the reduced solution $\mathbf{u}_{rb}$ is given by:

$$\mathbf{u}_h \simeq \mathbf{u}_{rb} = \mathbb{V}\mathbb{V}^T\mathbf{u}_h = \sum_{i=1}^{N_h}(\mathbb{V}\mathbb{V}^T\mathbf{u}_h)_i\phi_i = \sum_{j=1}^{L}(\mathbb{V}^T\mathbf{u}_h)_j\mathbf{w}_j. \tag{4.11}$$

The aim is to approximate the function:

$$\pi : \mu \in \mathbb{P} \longrightarrow \mathbb{V}^T\mathbf{u}_h \in \mathbb{R}^L, \tag{4.12}$$

with a neural network.
Once the approximated function $\bar{\pi}(\mu)$ is computed, the solution can be simply calculated for any parameter as $\mathbb{V}\bar{\pi}(\mu)$ during the online stage.
More in detail, the network will have an input layer of dimension given by the parameter vector μ, n hidden layers of the same dimension H and an output layer of dimension given by the function $\bar{\pi}(\mu)$.
The training set is constructed using random sampling in the parameter space. The performance of neural networks is affected by the range of the input, thus feature scaling needs to be performed before feeding the training data into the network. For the parameter μ, the mean $\bar{\mu}$ and the standard deviation σ_μ of the training data can be utilized to scale the input as follow [51]:

$$\mu = \frac{\mu - \bar{\mu}}{\sigma_\mu}. \tag{4.13}$$

Since it is a supervised learning method, in the training phase the goal will be to minimize the loss function defined as the mean squared error of the training data [40] [42].

4.3 Numerical Results

In this section, results for time and for stenosis degree reduction are shown. To avoid being repetitive, we choose the CABG1 configuration to test the ROM theory described before. Firstly, for simplicity, we set the stenosis degree and we look only the time as parameter, then we will consider both time and stenosis degree. Stenosis is introduced in our geometry thanks to mimmo C++ library for manipulation and morphing of surface and volume meshes (Figure 4.3). To compare results, it is important to warp the mesh and not only the geometry, so that the same number of cells is present in all geometries.

4.3.1 Computational time reduction

For this study, CABG1 with 50% stenosis is taken into account. Two hundred snapshots are collected with the FVM every $0.004s$ on a cardiac cycle, precisely between $1.6s$ and $2.4s$. POD modes are computed as explained in Chapter 4 using MATLAB. Figure 4.4

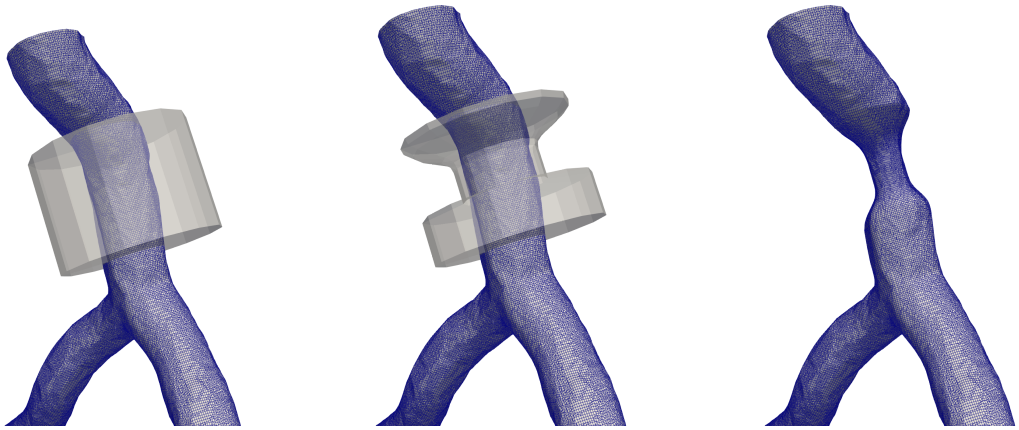

(a) Lattice. (b) Deformed lattice. (c) Stenosis 50%.

Figure 4.3: Introduction of the stenosis.

shows the cumulative energy of the eigenvalues for pressure p, wall shear stress WSS, and velocity magnitude U. The nth cumulative eigenvalues is computed as:

$$\frac{\sum_{i=1}^{n} \sigma_i}{\sum_{i=1}^{N} \sigma_i}, \tag{4.14}$$

where N is the total number of eigenvalues.

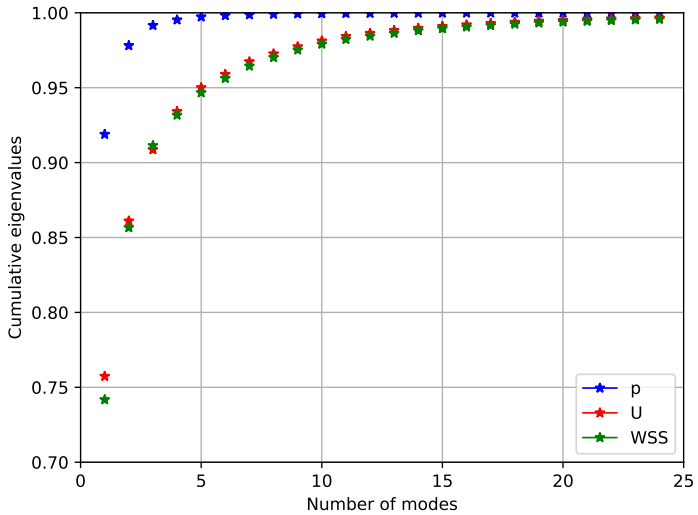

Figure 4.4: Cumulative eigenvalues in the case of time reduction.

In order to retain the 99% of the system energy, 3 modes for the pressure, 15 for the

velocity and 16 for the WSS are selected. Then, using *pytorch* library, we implement a neural network to compute the coefficients of the reduced solution. A POD-NN approach is deployed, taking as data the snapshots obtained with the FVM. Three different neural networks are trained respectively to find the pressure, the velocity and the WSS. In Table 4.1 are shown parameters used in the neural networks. In all cases, the input dimension of the network is 1, the output dimension is equal to the number of modes selected, the hidden layers are 3, the optimizer with the best performance is the Adam optimizer and the loss function measures the mean square error (MSE). In addition, all data are scaled to zero mean and unit variance. The combinations of these parameters exhibit a good

	Neurons per layer	Activation function	Number of epochs	Learning rate
p	500	ReLU	50.000	1.00e-6
U	850	Tanh	100.000	8.25e-6
WSS	900	Tanh	100.000	5.50e-6

Table 4.1: Parameters of the NNs for time reduction.

performance, as the loss and the accuracy trend indicate in Figure 4.5 and 4.6. The test set is 5% of the whole data set and the over-fitting phenomenon is absent at the end of the training because the curves in Figure 4.6 are close each other. For completeness, in Figure 4.6a the test accuracy at the end of the training is about 96%, in 4.6b is about 92% and in 4.6c it is about 95%.

Even if the test accuracy is not 100%, it is high enough to reach satisfactory results, as validated in Figure 4.7. In these graphs, we show some coefficients of the reduced solution and red points (i.e. test points) are consistent with training data.
In addition, the following figures display a qualitative comparison between full order model (FOM) and reduced order model (ROM) at test time $1.832s$. Figure 4.8 indicates on the whole a good estimate of the pressure with POD-NN. It is also confirmed in Figure 4.9 and 4.10, where the pressure at the junction LITA-LAD and downstream of the stenosis is shown.

ROM is able to provide a good reconstruction also for the WSS, as proved in Figure 4.11, 4.12 and 4.13. In addition, it can be seen that a region of high WSS is located around the anastomosis.

In order to investigate the flow field, velocity streamlines in Figure 4.14, 4.15 and 4.16 are obtained using 500 points with a random sampling. In addition, a slice in the region of the stenosis shows the internal velocity field in Figure 4.17. It appears that the velocity is higher in the LITA and in general in the central region of the vessel, decreasing to 0 on the boundary as enforced by no slip condition.

From a quantitative point of view, relative errors of the reduced solutions are shown in Figure 4.18, in addition the maximum, the minimum and the mean of the errors can be seen in Table 4.2. They show overall a good performance of the method.

Lastly for completeness, the time of the online phase, SVD analysis time, training time of the networks, the speed up and the time required for high fidelity simulations can be found in Table 4.3. To be clear, the snapshots are obtained from SISSA/ICTP supercomputer on 20 processors.

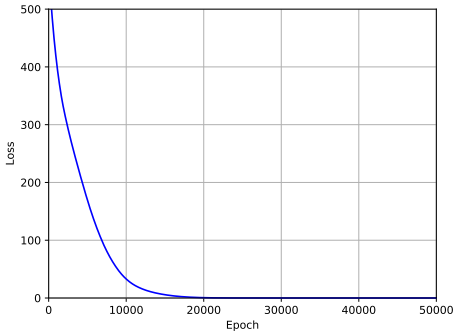

(a) p loss.

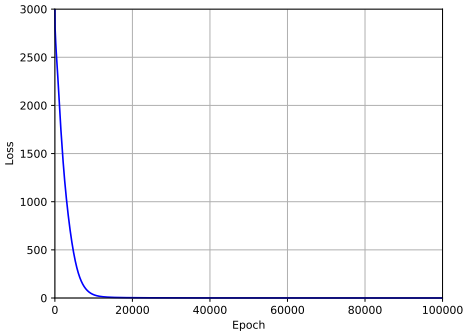

(b) WSS loss.

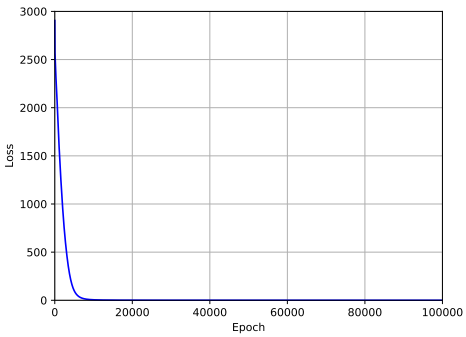

(c) U loss.

Figure 4.5: Loss trend in the case of time reduction.

	Max	Min	Mean
p	0.15660649	0.0012431271	0.017409940
U	0.069776229	0.0010527188	0.0089876854
WSS	0.073688335	0.0010436620	0.010549063

Table 4.2: Maximum, minimum and mean of the relative errors in the case of time reduction.

4.3.2 Variation in the degree of the stenosis

In order to generalize the previous analysis, we consider CABG1 configuration with degree of stenosis from 50% to 75% with step 5. Two hundred snapshots are collected for each geometry with the FVM every $0.004s$ on a cardiac cycle (between $1.6s$ and $2.4s$). So, we construct a matrix with 986.278 rows for p and U (193.625 for WSS) and $6 \times 200 = 1200$ columns (snapshots) in order to extrapolate POD modes. Due to the large size of the matrix, we compute only the first one hundred cumulative eigenvalues and left eigenvectors

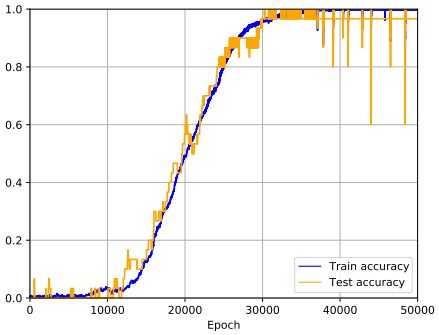

(a) p accuracy.

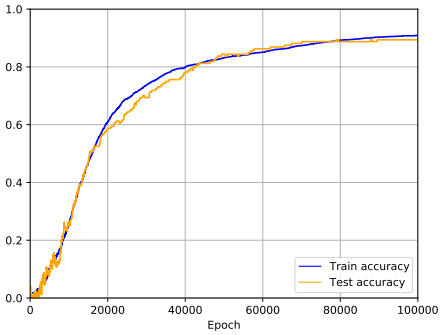

(b) WSS accuracy.

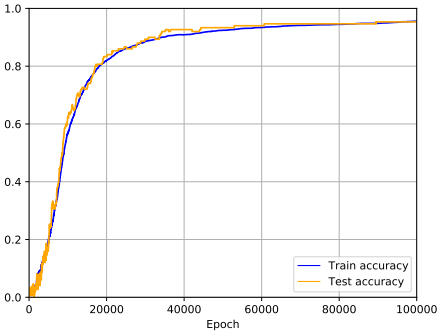

(c) U accuracy.

Figure 4.6: Train-test accuracy in the case of time reduction.

	$t_{online}[s]$	$t_{SVD}[s]$	$t_{training}[s]$	Speed up	$t_{FOM}[s]$
p	8.778422832	180.8203177	895.0288848	3.350214561e5	147048×20
U	10.70492005	350.0547475	3209.481549	2.747297491e5	
WSS	2.072308063	21.33345222	2406.573431	1.419171238e6	

Table 4.3: Time required for some stages of the time reduction.

with the python library *sklearn.decomposition.TruncatedSVD*. In this case, 3 and 10 modes for the pressure are sufficient in order to reach respectively the 99% and 99.9% of the system energy. For the pressure, it is necessary to consider 10 modes in order to reach satisfactory results because otherwise the error of the reduced solution exhibited in Figure 4.20c is too high. For the velocity, 29 and 79 modes need to reach 99% and 99.9% of the system energy. So, due to the huge number of modes and due to the reasonable error trend in Figure 4.20a, we choose to keep 29 modes to find the reduced solution. Finally, for the WSS, 29 and 80 modes are used to get to 99% and 99.9% of the system energy. Similar to the velocity, 29 modes are considered for the study. The maximum, the

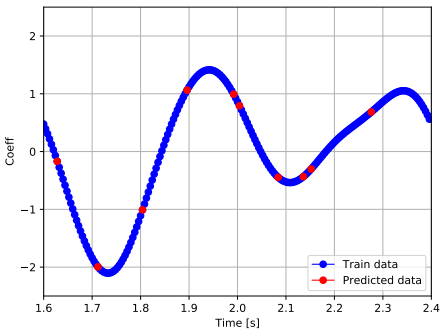

(a) 1st coefficient of p.

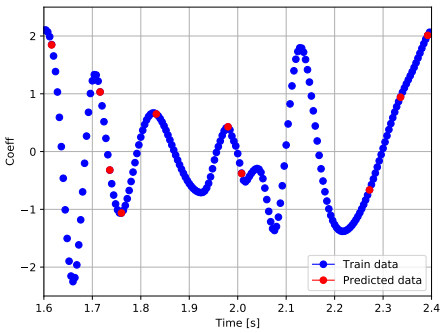

(b) 11th coefficient of WSS.

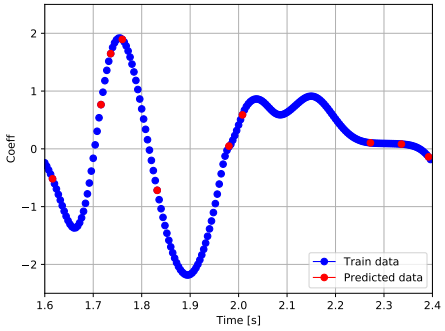

(c) 4th coefficient of U.

Figure 4.7: Modal coefficients of the reduced solutions in time.

minimum and the mean of the errors can be found in Table 4.4. Due to the increase of the parameters, the errors are greater compared to the previous case. The maximum of the relative error shows that the model is not able to reproduce properly the truth solution around the time $2s$, whereas for the others time steps the method performs well.

	Max	Min	Mean
p - 3 modes	2.370129	0.0035572464	0.12618929
p - 10 modes	0.40112498	0.000935177	0.028314954
U	0.3500804	0.0031757178	0.03131248
WSS	0.35365012	0.0038626634	0.055840865

Table 4.4: Maximum, minimum and mean of the relative errors with the stenosis as parameter.

Cumulative eigenvalues for p, U and WSS are shown in Figure 4.19.

As before, a neural network model is trained to predict the coefficients of the reduced

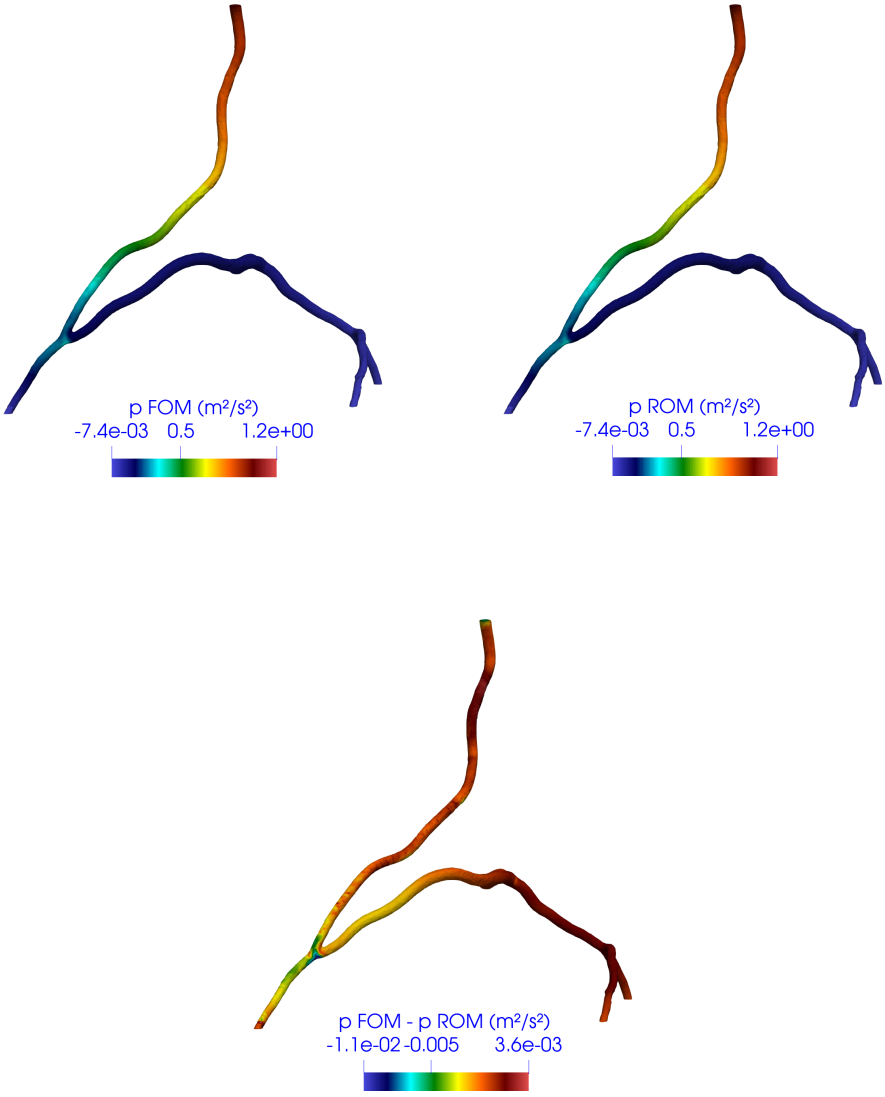

Figure 4.8: Comparison of FOM/ROM pressure in the case of time reduction.

solutions. Three different neural networks are trained respectively to find the pressure, the velocity and the WSS. In particular, a single neural network is used to predict the coefficients for all geometries under examination. The input dimension of the network is 2 (as the parameters) and the output dimension is equal to the number of modes selected. In particular, we choose data corresponding to 70% of stenosis as test, so these data are not included in the training phase. In Table 4.5 are shown parameters used to train the

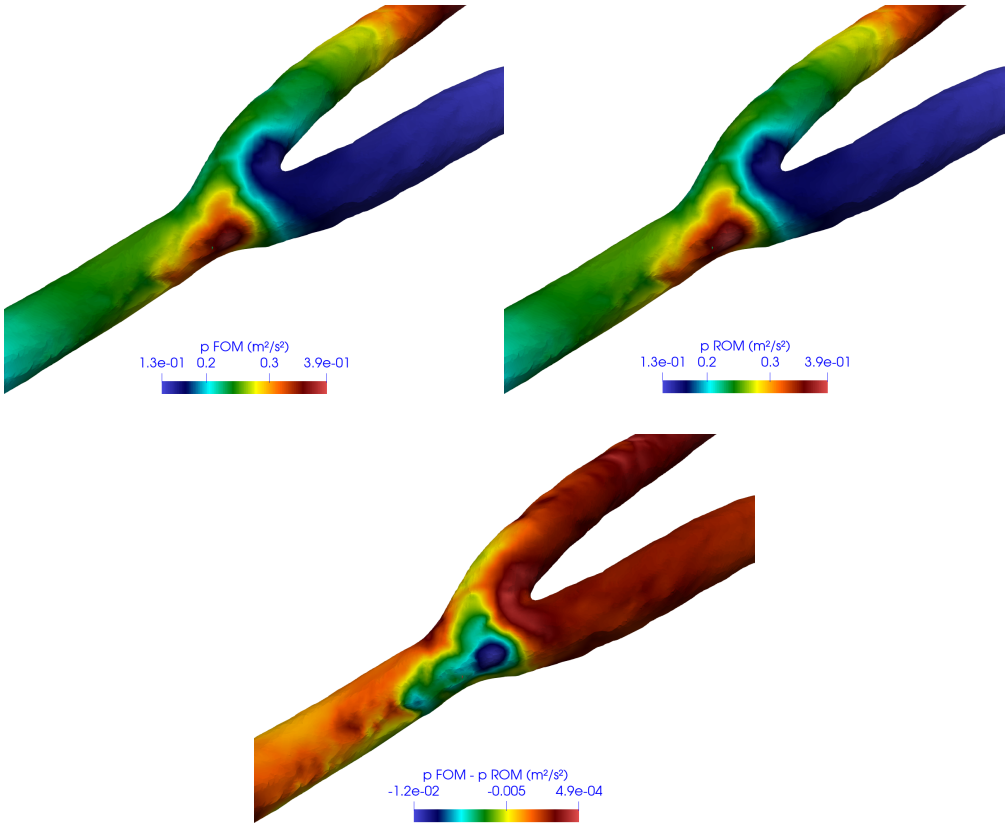

Figure 4.9: Comparison of FOM/ROM pressure at the graft junction in the case of time reduction.

networks. What is not specified here is the same of the previous section.

	Neurons per layer	Activation function	Number of epochs	Learning rate
p	1300	Tanh	50.000	8.25e-6
U	1300	Sigmoid	100.000	5.00e-5
WSS	1300	Tanh	100.000	8.50e-6

Table 4.5: Parameters of the NNs with the stenosis as parameter.

Loss and accuracy trend can be found in Figure 4.21 and 4.22. In this case, for the pressure the final test accuracy is about 93%, for the WSS and for the velocity it is about 88%. A slight overfitting can be seen in Figure 4.22b and 4.22c, but it does not introduce issues.

In fact, as support to the functionality of the networks, some coefficients of the reduced solutions are presented in Figure 4.23, where test points are consistent with training data.

Again, from a qualitative point of view, the pressure at test time 1.832s and 70%

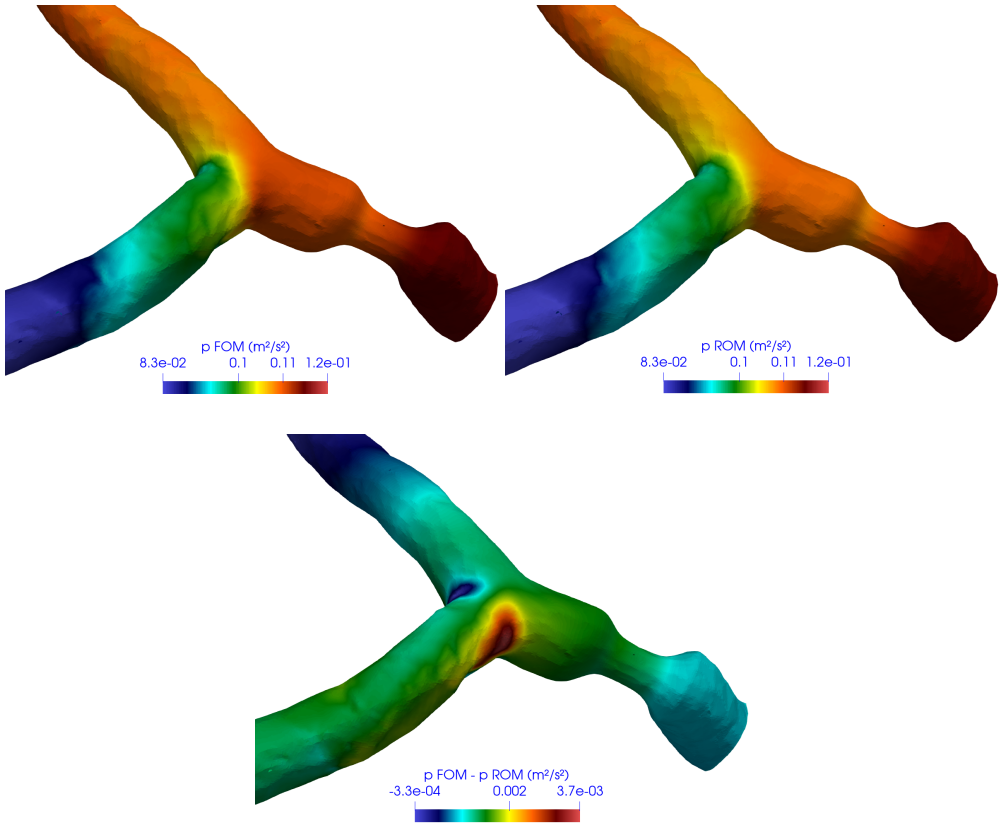

Figure 4.10: Comparison of FOM/ROM pressure near the stenosis in the case of time reduction.

stenosis is shown in Figure 4.24. Also the region of the graft and the region of the stenosis in Figure 4.25 and 4.26 exhibits successful results.

In Figure 4.27, it can be appreciated a vary similar distribution of the WSS on the wall domain. It can be seen also in Figure 4.28 and 4.29, where the usual details of the geometry are displayed.

In this case, it is attractive to remark that, in the region of the graft, WSS distributions for stenosis 50% and 70% in Figure 4.30a and 4.30b are similar. However, due to the higher velocity imposed on the LITA, the WSS reaches a greater value when 70% stenosis occurs. It is reflected at the beginning of the LAD and LCx as well (Figure 4.31).

In order to investigate the flow field, velocity streamlines can be found for the whole geometry, for the graft and for the stenosis in Figure 4.32, 4.33 and 4.34. In addition, in the region of the stenosis, it can be seen the internal velocity field in Figure 4.35.

Consistently with the Figure 4.30 and 4.31, also the velocity achieves greater values when the obstruction increases. It can be noted both near the anastomosis and the stenosis (Figure 4.36 and 4.37).

All these graphs show that it is possible to use the ROM in order to obtain accurate

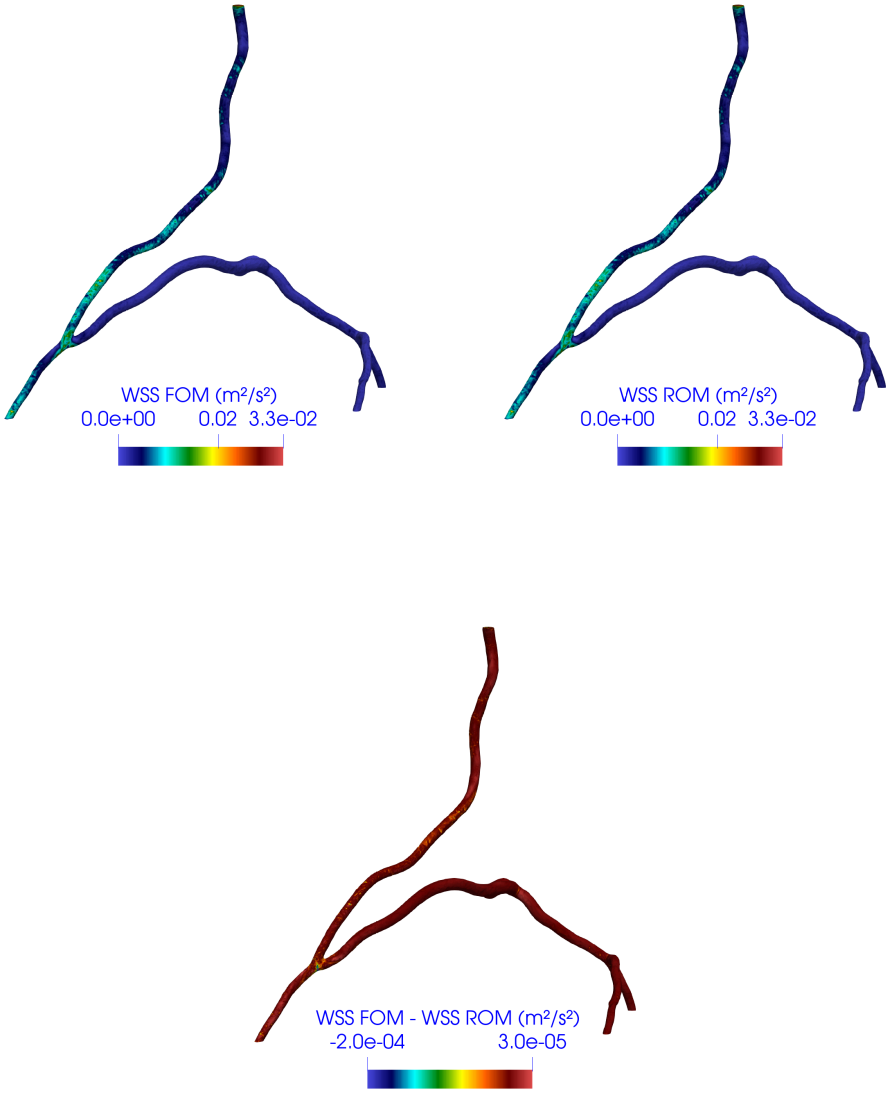

Figure 4.11: Comparison of FOM/ROM WSS in the case of time reduction.

simulations with a significant reduction of the computational cost. It is highlighted in Table 4.6, where training time of the networks, the time required for the online phase, SVD analysis time, the speed up and the time required for the high fidelity simulations can be found.

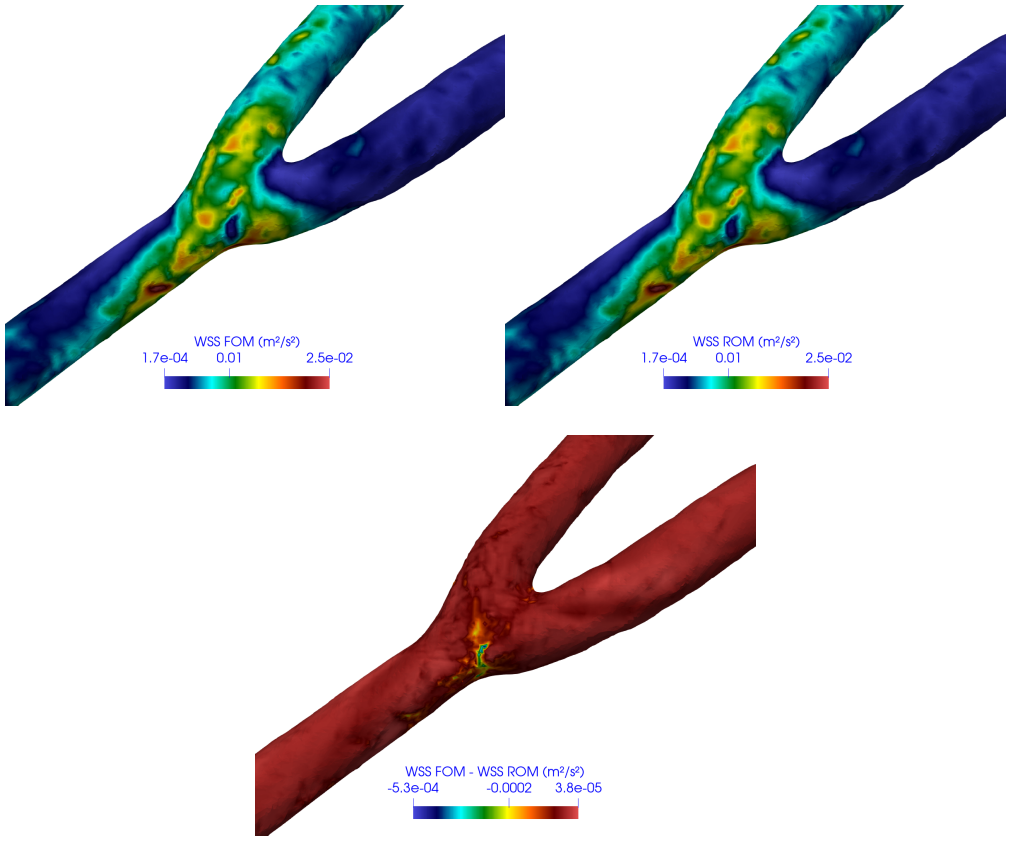

Figure 4.12: Comparison of FOM/ROM WSS at the graft junction in the case of time reduction.

	$t_{online}[s]$	$t_{SVD}[s]$	$t_{training}[s]$	Speed up	$t_{FOM}[s]$
p	5.426410198	2371.641028	13182.88197	5.419715599e5	147048 × 20
U	9.416581153	2827.823787	24545.71179	3.123171724e5	
WSS	1.695662517	10.73292016	25118.61685	1.734401728e6	

Table 4.6: Time required for some stages with the stenosis as parameter.

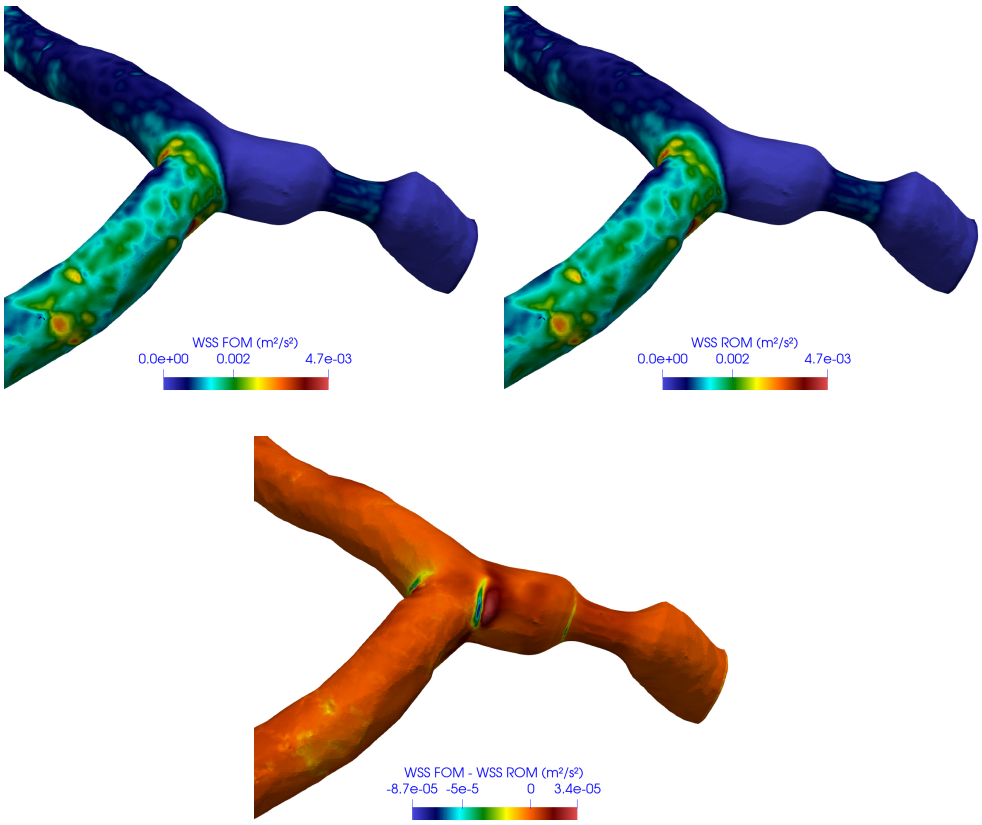

Figure 4.13: Comparison of FOM/ROM WSS near the stenosis in the case of time reduction.

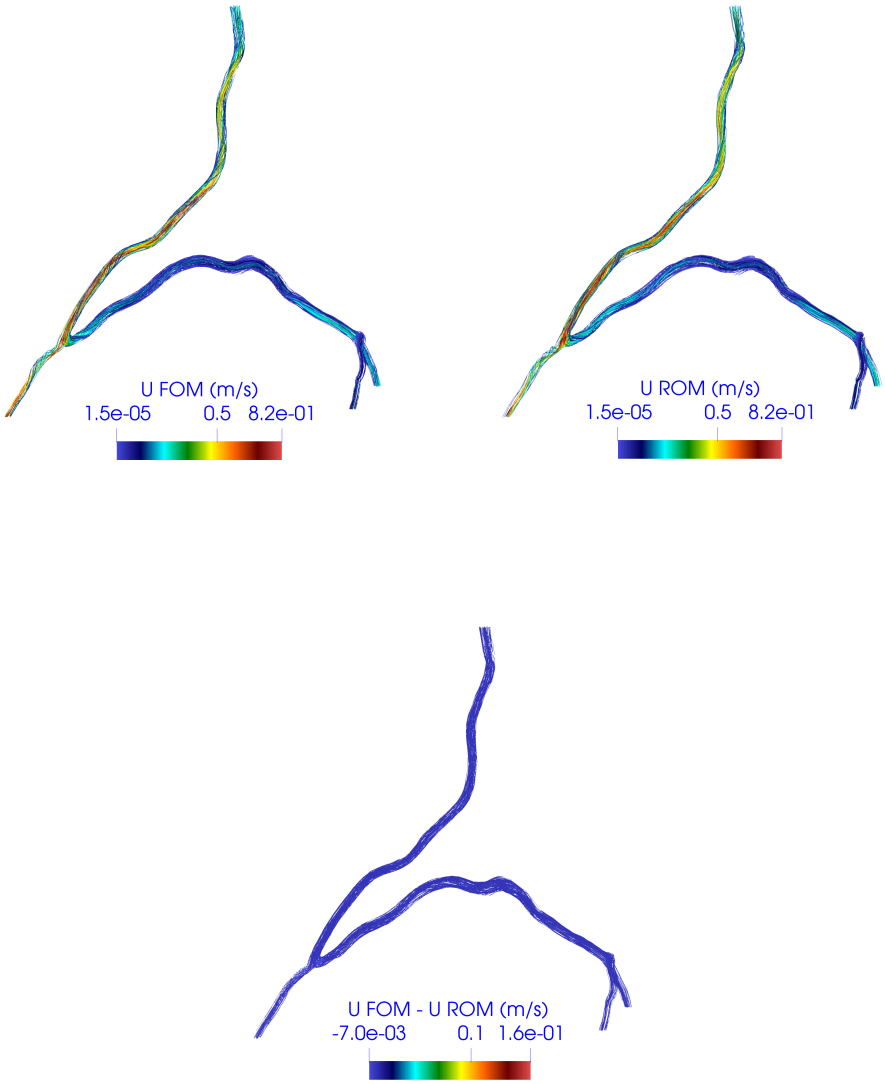

Figure 4.14: Comparison of FOM/ROM streamlines in the case of time reduction.

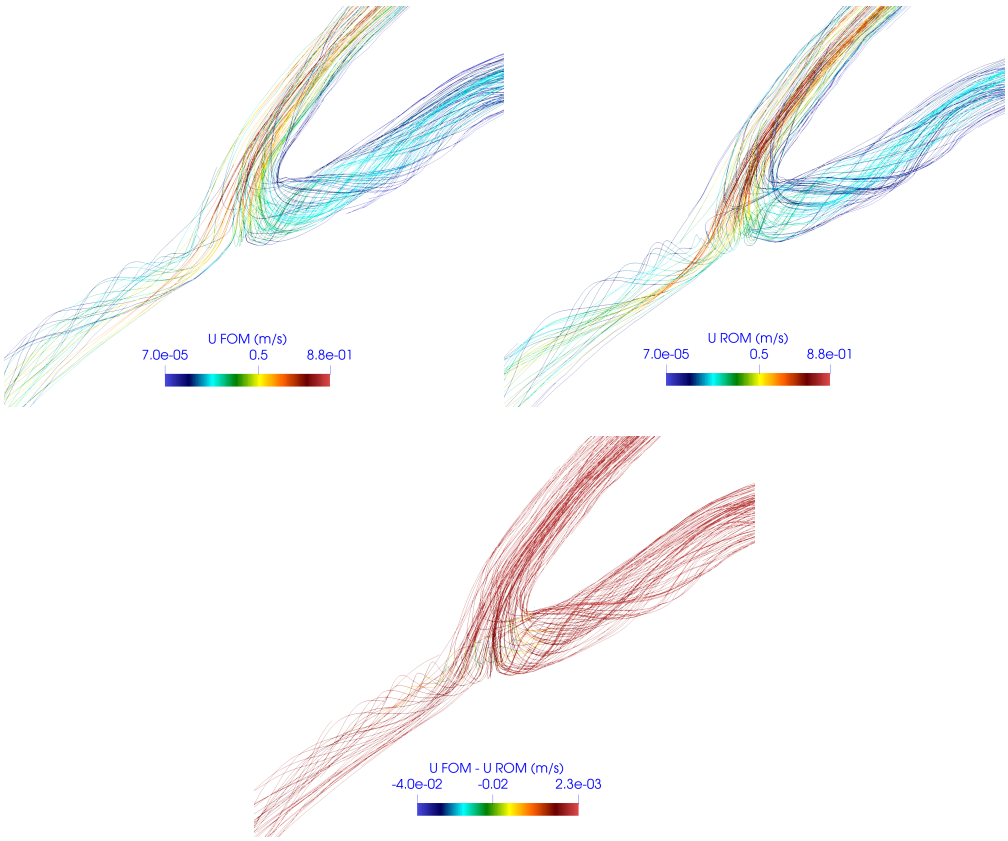

Figure 4.15: Comparison of FOM/ROM streamlines at the graft junction in the case of time reduction.

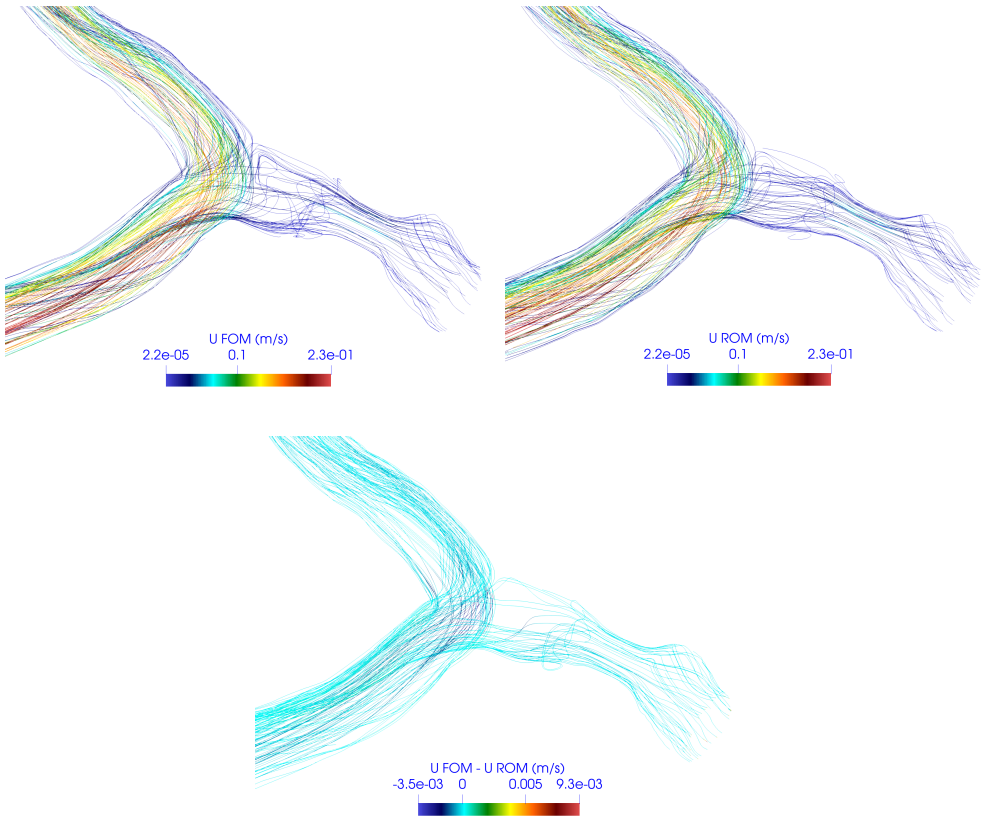

Figure 4.16: Comparison of FOM/ROM streamlines near the stenosis in the case of time reduction.

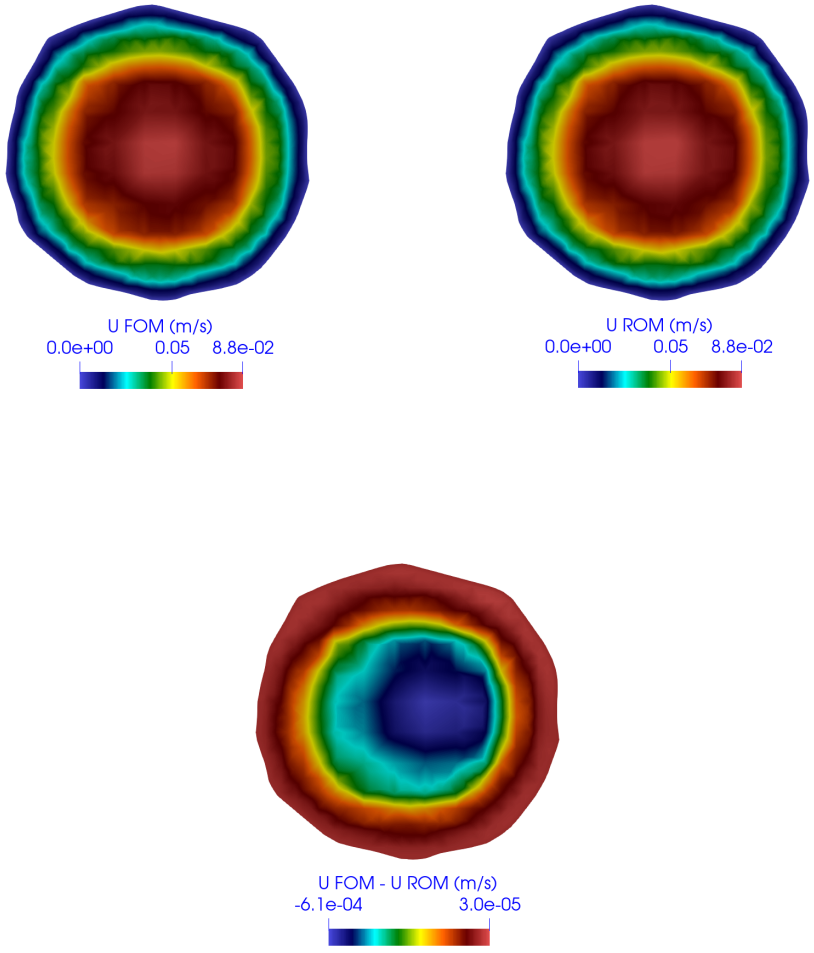

Figure 4.17: Comparison of FOM/ROM internal velocity in the case of time reduction.

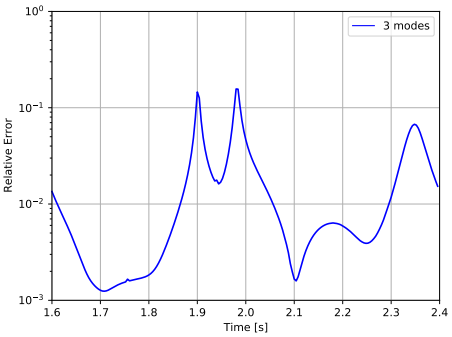

(a) p error.

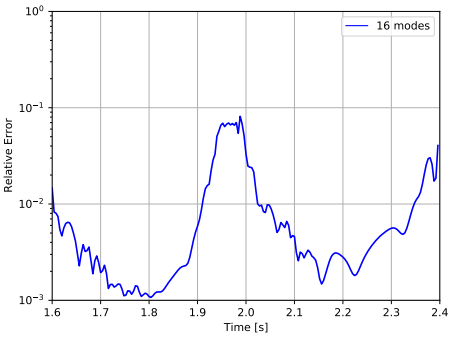

(b) WSS error.

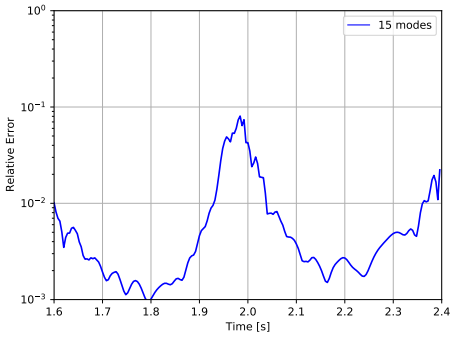

(c) U error.

Figure 4.18: Error trend over time in the case of time reduction.

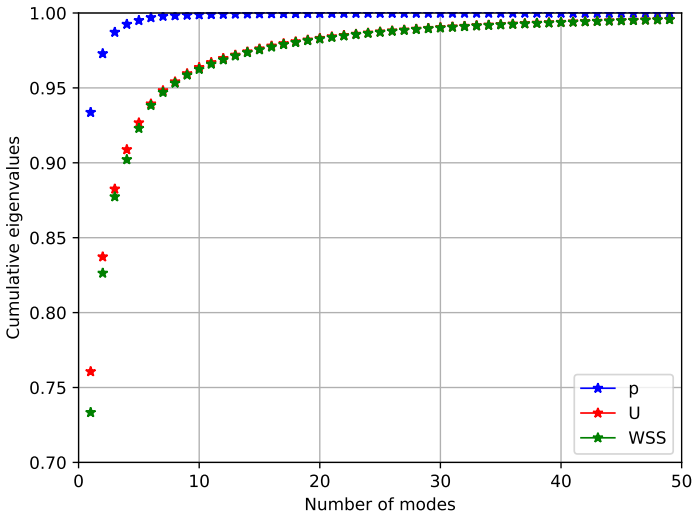

Figure 4.19: Cumulative eigenvalues with the stenosis as parameter.

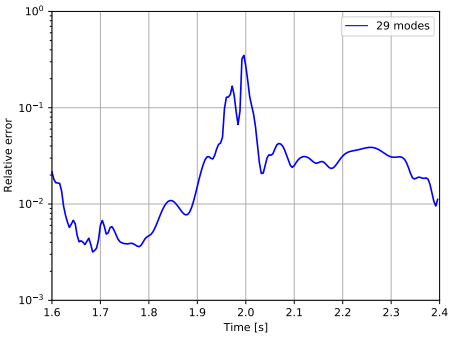

(a) U error.

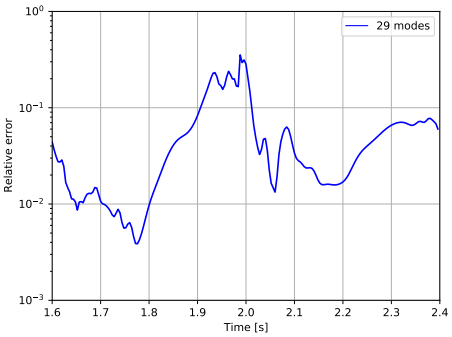

(b) WSS error.

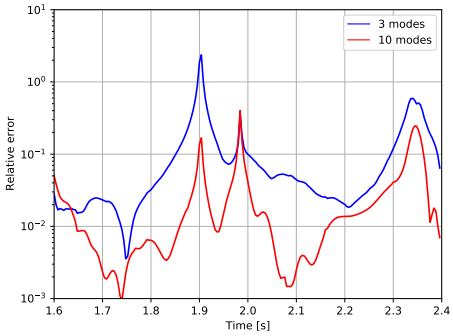

(c) p error.

Figure 4.20: Error trend over time in the case stenosis 70%, chosen as test sample.

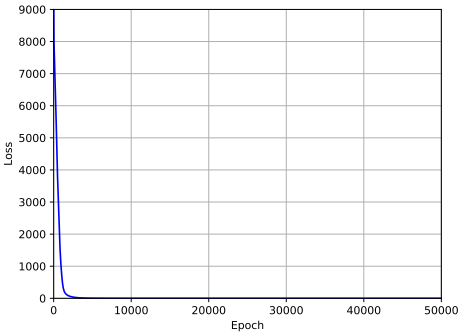

(a) p loss.

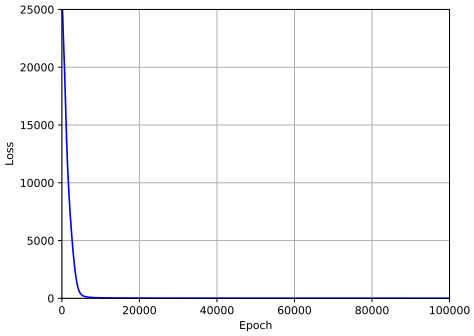

(b) WSS loss.

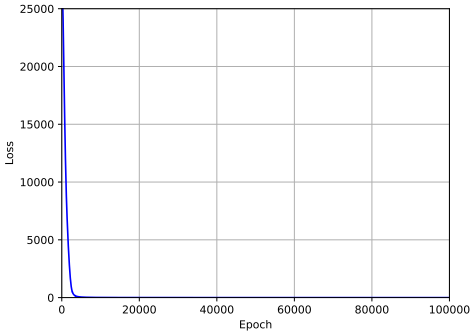

(c) U loss.

Figure 4.21: Loss trend with the stenosis as parameter.

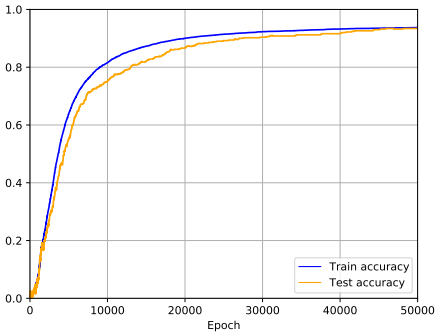

(a) p accuracy.

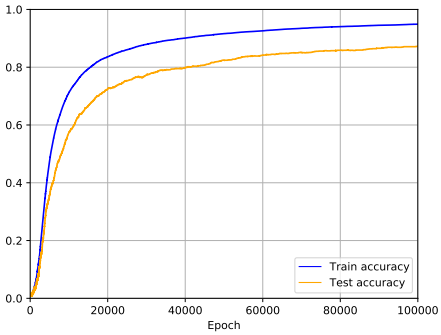

(b) WSS accuracy.

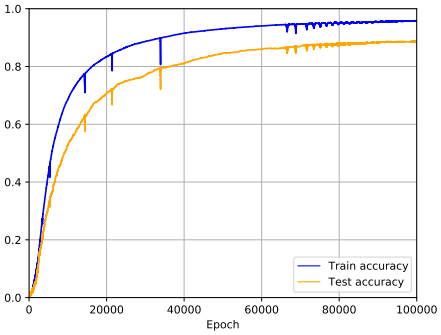

(c) U accuracy.

Figure 4.22: Train-test accuracy with the stenosis as parameter.

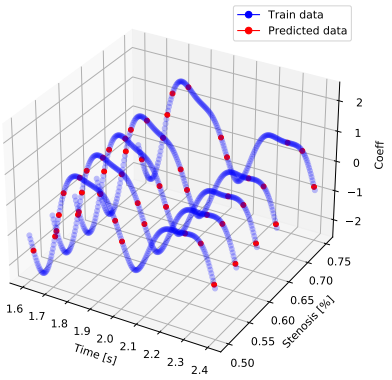

(a) 3rd coefficient of p.

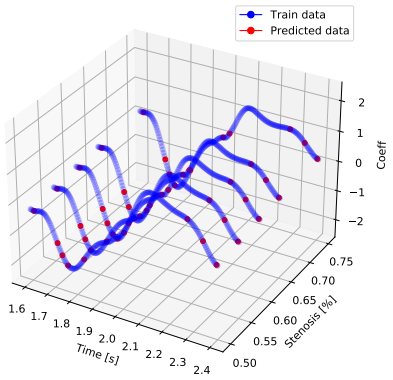

(b) 2nd coefficient of WSS.

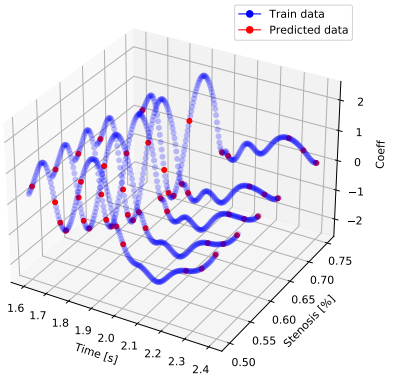

(c) 4th coefficient of U.

Figure 4.23: Modal coefficients of the reduced solutions with the stenosis as parameter.

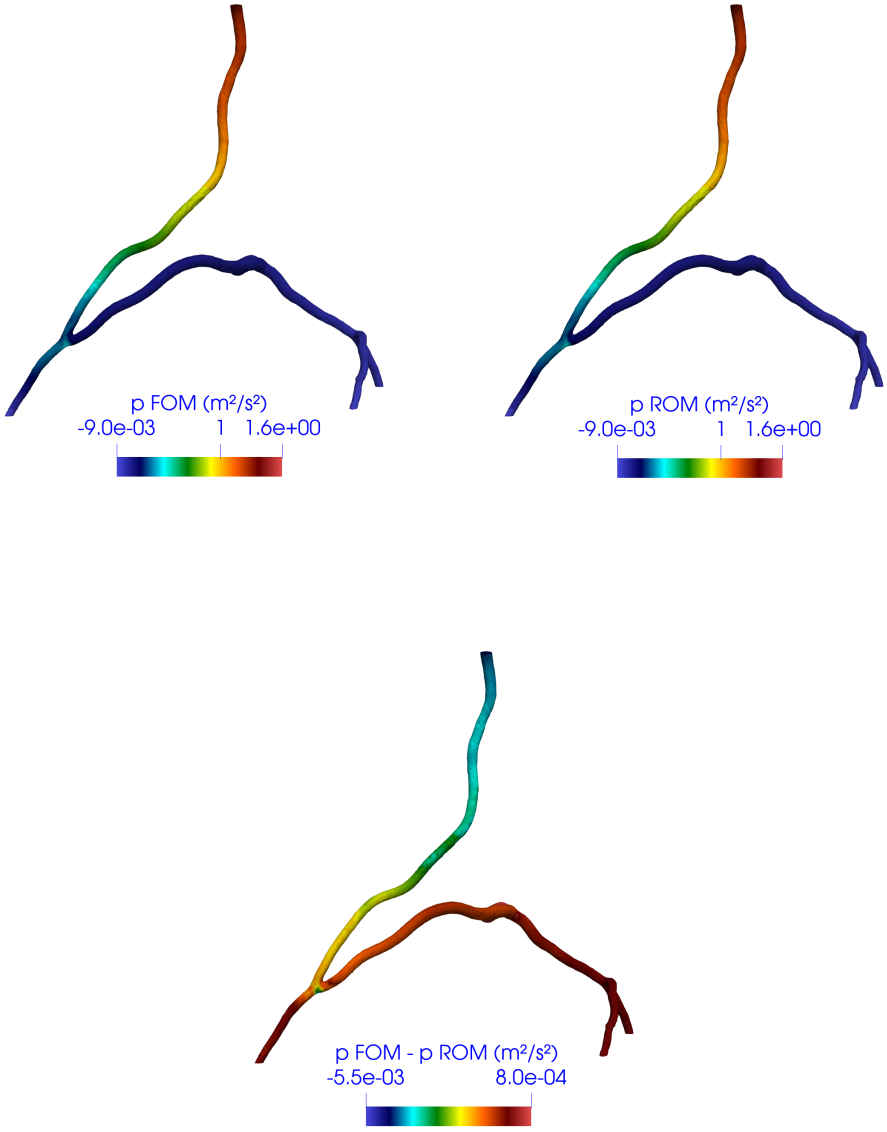

Figure 4.24: Comparison of FOM/ROM pressure with the stenosis as parameter.

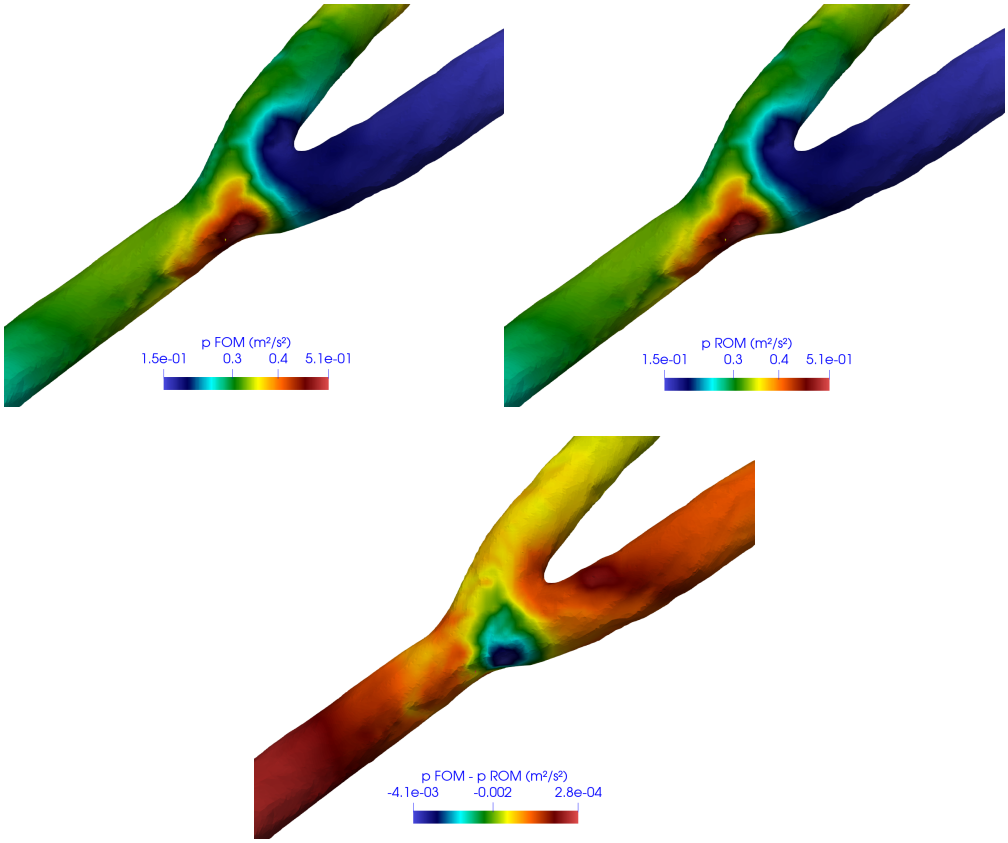

Figure 4.25: Comparison of FOM/ROM pressure at the graft junction with the stenosis as parameter.

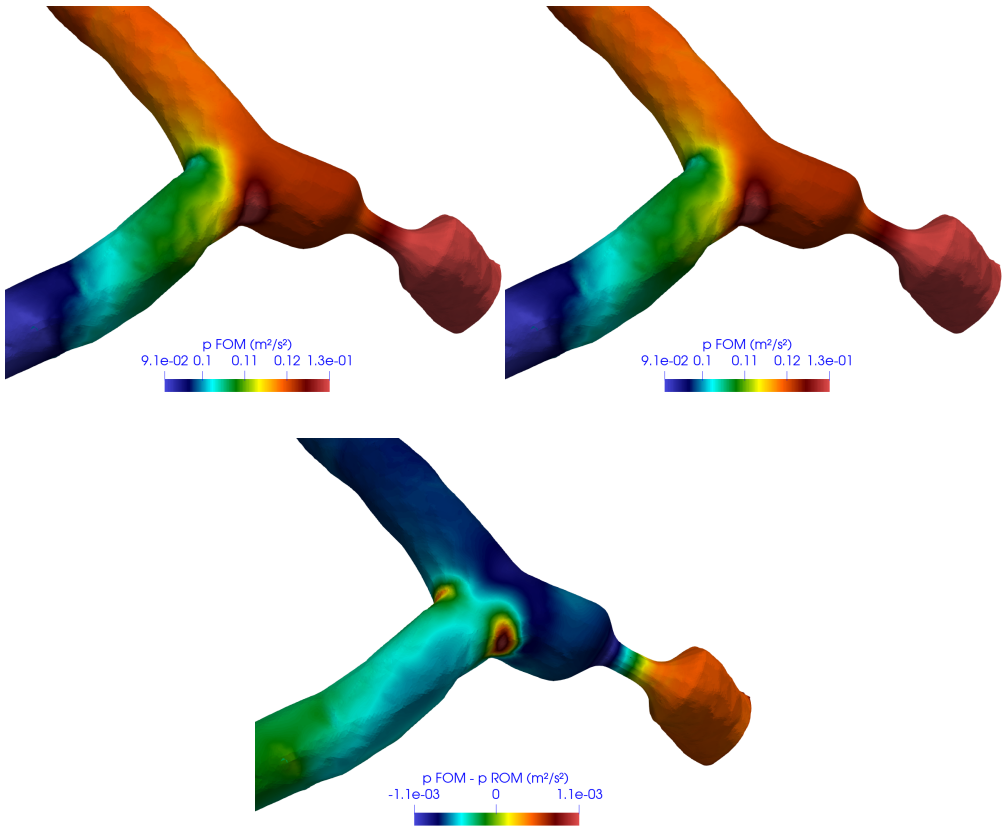

Figure 4.26: Comparison of FOM/ROM pressure near the stenosis with the stenosis as parameter.

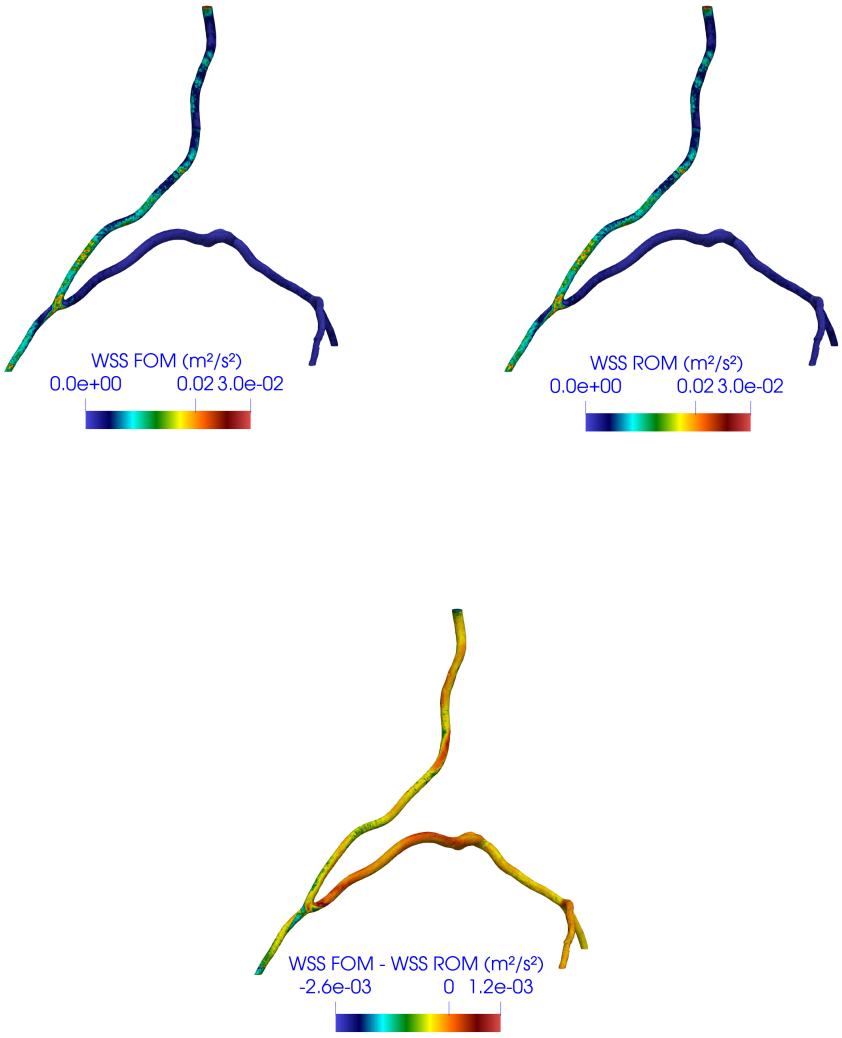

Figure 4.27: Comparison of FOM/ROM WSS with the stenosis as parameter.

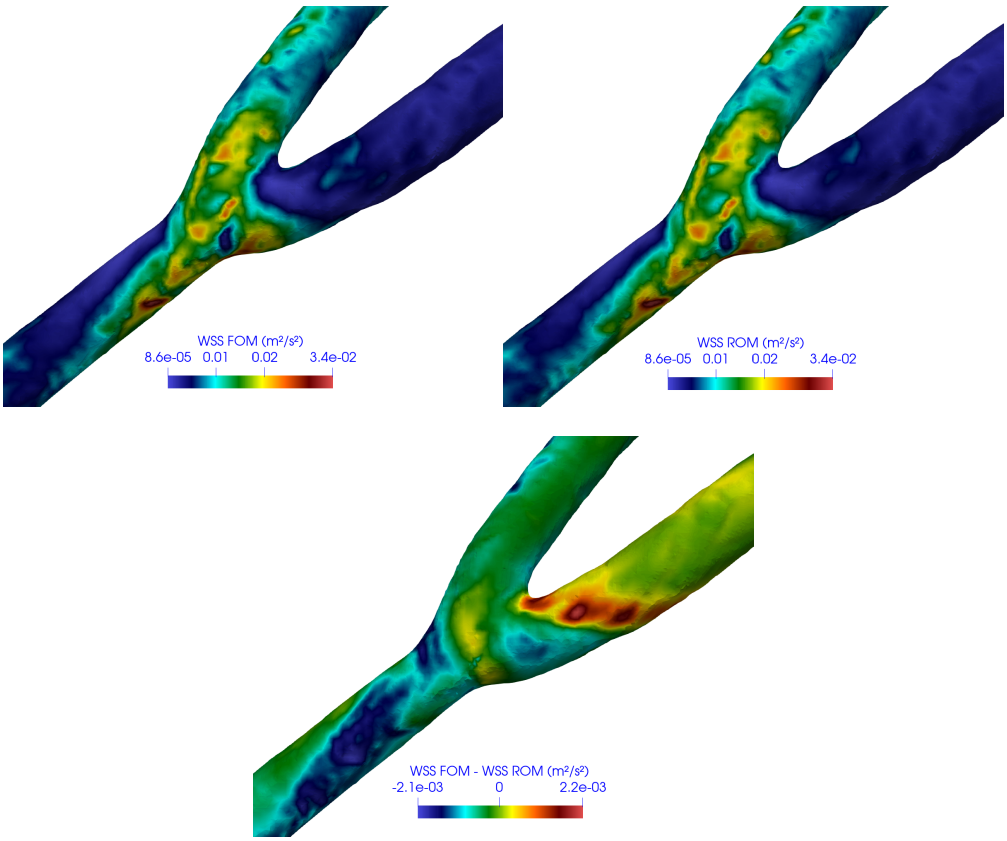

Figure 4.28: Comparison of FOM/ROM WSS at the graft junction with the stenosis as parameter.

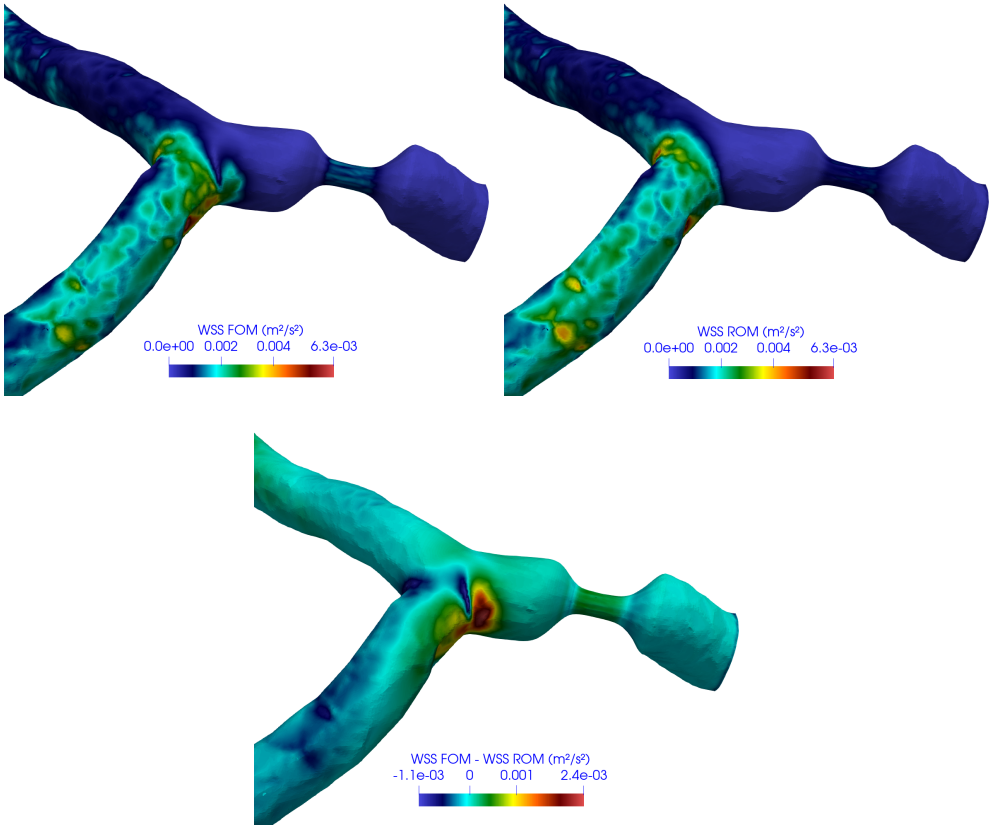

Figure 4.29: Comparison of FOM/ROM WSS near the stenosis with the stenosis as parameter.

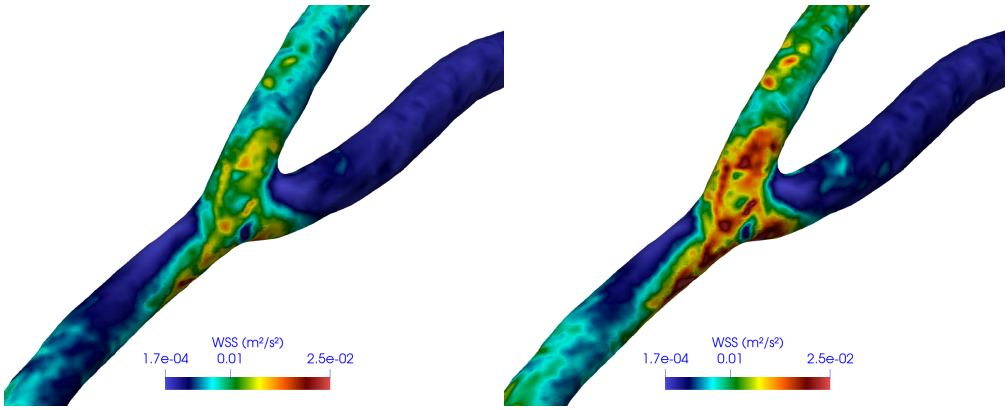

(a) 50% stenosis. (b) 70% stenosis.

Figure 4.30: Comparison of WSS between 50% and 70% stenosis near the junction.

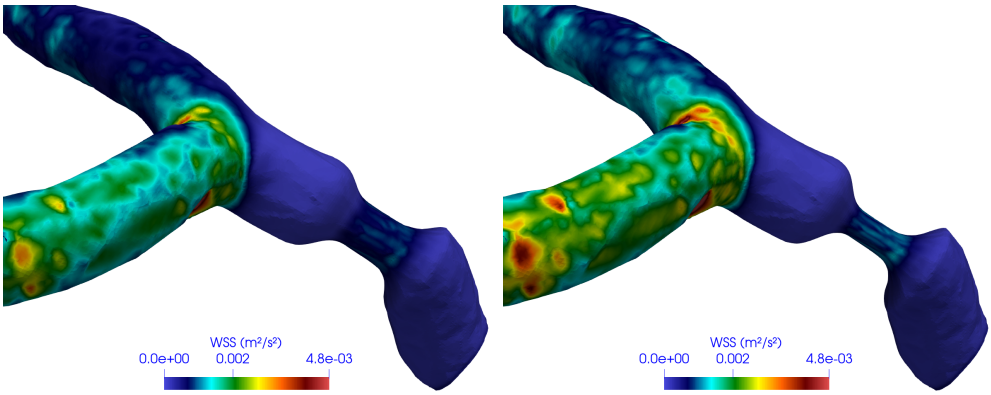

(a) 50% stenosis.

(b) 70% stenosis.

Figure 4.31: Comparison of WSS between 50% and 70% stenosis near the stenosis.

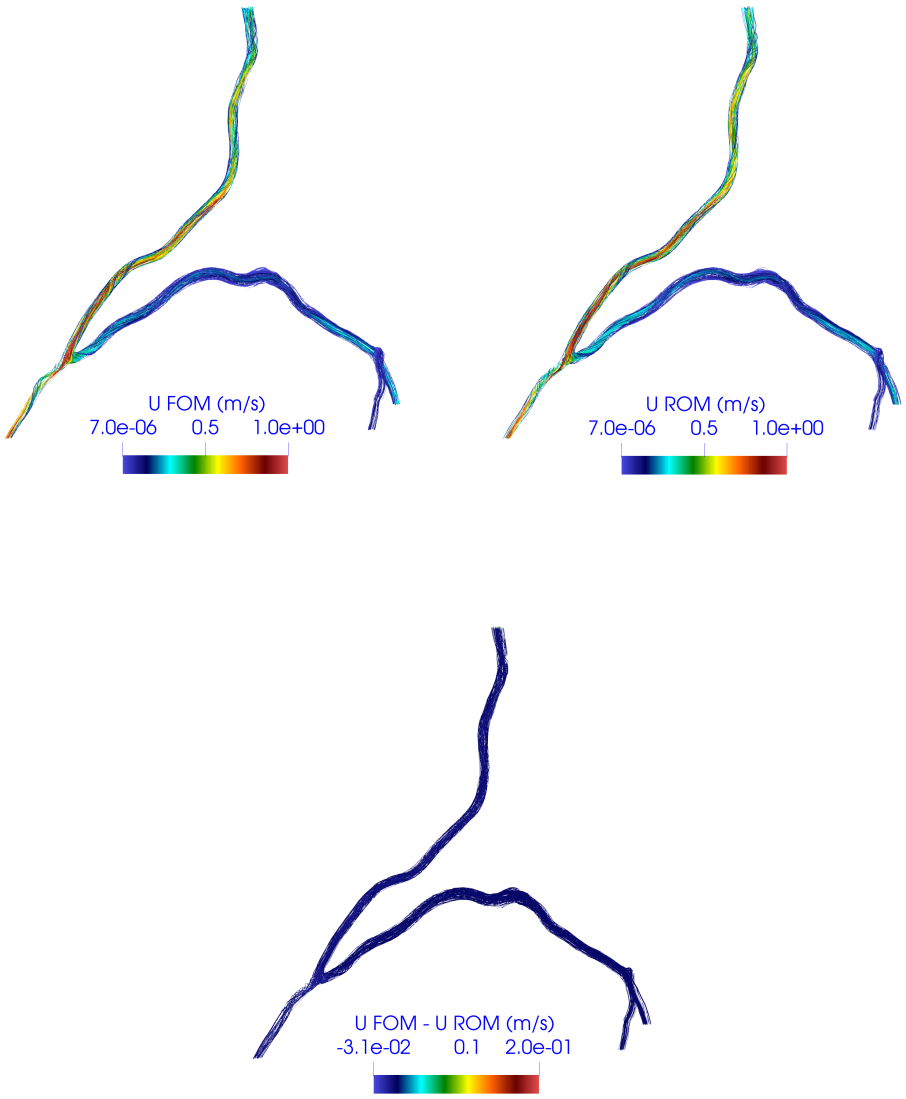

Figure 4.32: Comparison of FOM/ROM streamlines with the stenosis as parameter.

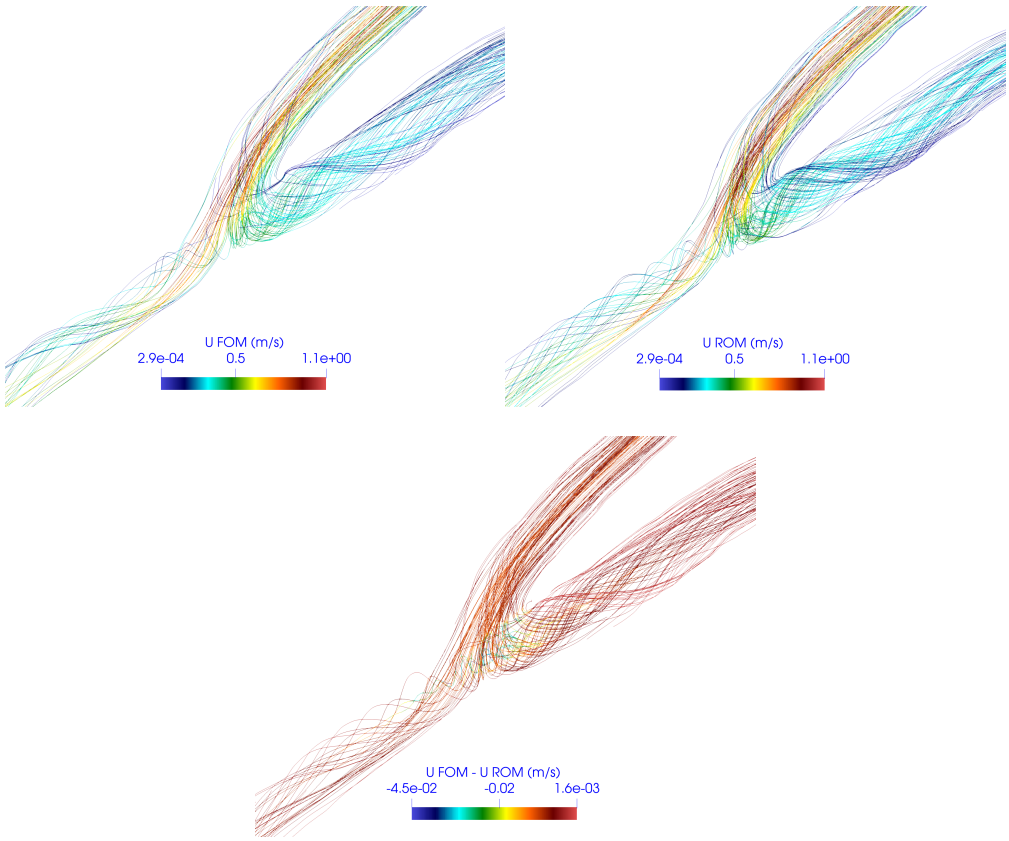

Figure 4.33: Comparison of FOM/ROM streamlines at the graft junction with the stenosis as parameter.

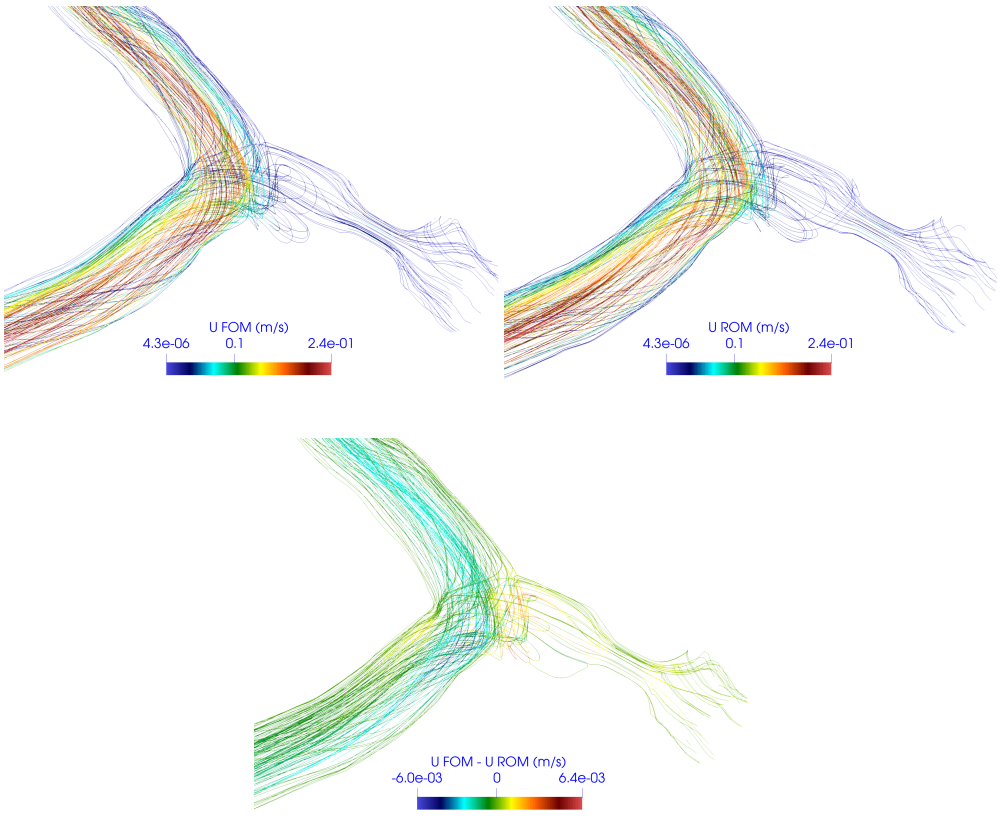

Figure 4.34: Comparison of FOM/ROM streamlines near the stenosis with the stenosis as parameter.

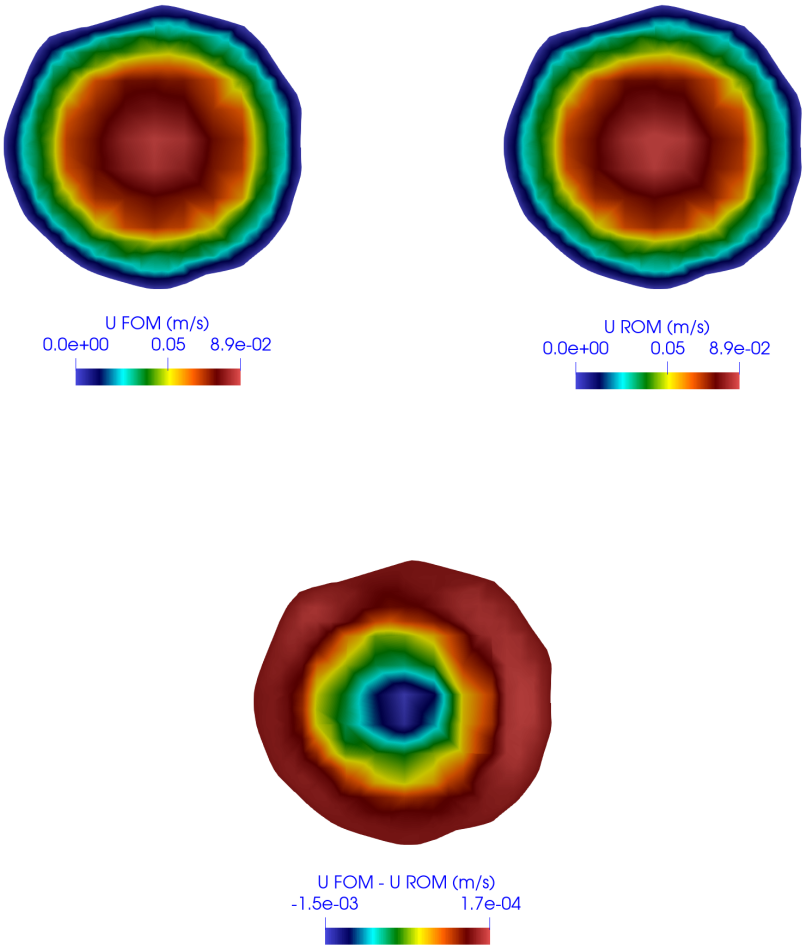

Figure 4.35: Comparison of FOM/ROM internal velocity with the stenosis as parameter.

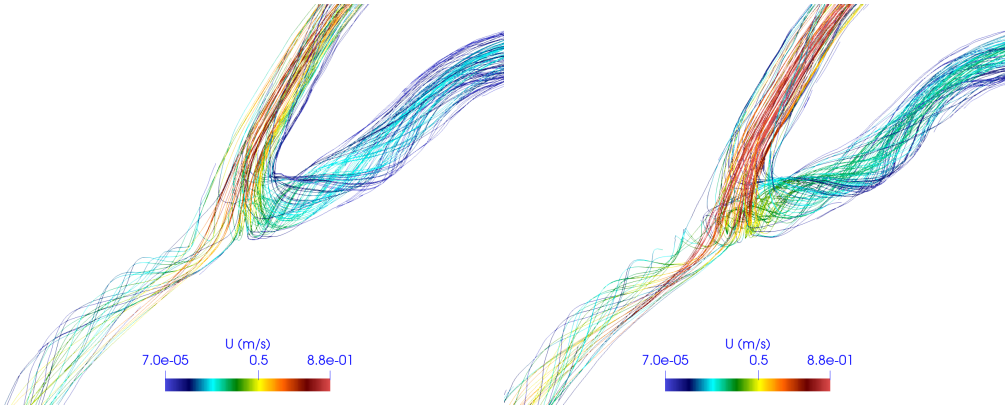

(a) 50% stenosis. (b) 70% stenosis.

Figure 4.36: Comparison of U between 50% and 70% stenosis near the junction.

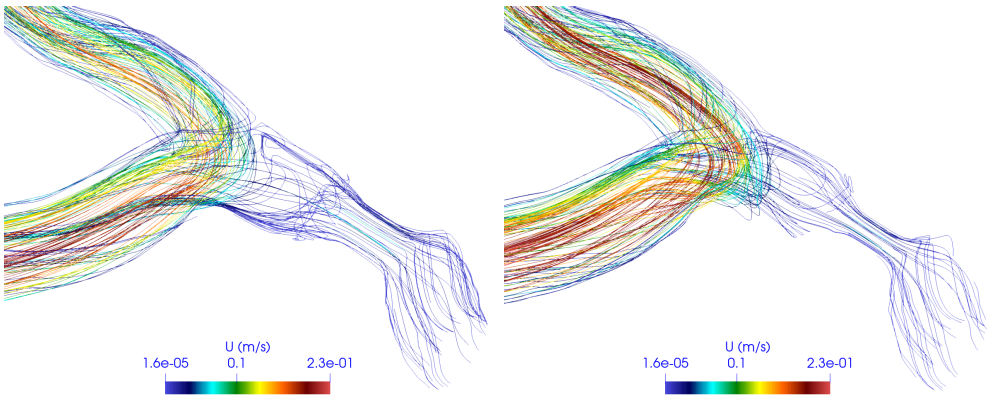

(a) 50% stenosis. (b) 70% stenosis.

Figure 4.37: Comparison of U between 50% and 70% stenosis near the stenosis.

Conclusion and perspectives

In this work, a non-intrusive ROM using POD-NN method is employed in order to investigate the blood flow in coronary arteries when a stenosis of the LMCA occurs. The proposed framework has been applied to a patient-specific CABG configuration. As a first case, we considered only the time as parameter, than the degree of the stenosis from mild to severe is added too. The goal of the thesis is to verify the solid performance of the method for a complex geometry by using a data-driven analysis.
Incompressible Navier-Stokes equations are the starting point, then the FVM is used to find the so called high fidelity solutions. For the velocity, we have used boundary conditions which try to capture as much as possible the physiology of vascular networks outside of the domain. In all cases, after a computationally intensive offline stage performed on HPC architectures, POD-NN method has allowed to obtain haemodynamic simulations at greatly reduced computational costs. In addition, this ROM allows to obtain very accurate distributions on the whole domain for the variables considered, i.e. pressure, velocity and WSS.
However several improvements are possible for the proposed framework and in the study of patient-specific coronary artery bypass grafts. In order to obtain better results, it could be interesting to introduce a Windkessel RCR model. It could help us to improve boundary conditions, which represent a crucial step to obtain meaningful outcomes.
Due to covid emergency, we could not receive the geometry by Sacco hospital in Milan. So, we have modified another domain removing some branches and adding stenosis, in order to obtain the configurations of interest for the medical staff. The first (CABG1) is a bypass performed with the LITA on the LAD, while the second (CABG2) uses ad additional graft of SV from the LITA on the LCx.
The ROM theory has been successfully tested only for the configuration CABG1, therefore in the future it could be interesting to involve CABG2 too and as soon as possible it would be attractive to compare these two configurations with the help of the medical specialists, in order to understand which is the best choice from a practical point of view.
In this work, firstly we have considered only the time as parameter to test the reduced method and it performs well. When we introduce the stenosis as parameter, the error of the reduced solution rises. Even if it is popular that more parameters mean higher error, it could be investigated better the parameterization with the aim of reducing the difference between FOM and ROM solution. Basically for example, we can use more data in term of the degree of the stenosis and we can observe if the error of the reduced solution decreases. In addition, in order to explore the training process of the networks,

used to find the coefficients of the reduced solution, it could be interesting to implement a POD-PINN approach and to compare POD-PINN and POD-NN in terms of time and accuracy.

Bibliography

[1] L. Formaggia, A. Quarteroni, A. Veneziani, *Cardiovascular mathematics modeling and simulation of the circulatory system*, Springer science & business media, 1, 2009.

[2] S. Chien, S. Usami, R. J. Dellenback, M. I. Gregersen, *Blood viscosity influence of erythrocyte aggregation*, Science, 157(3790), 829-831, 1967.

[3] B. M. Johnston, P. R. Johnston, S. Corney, D. Kilpatrick, *Non-Newtonian blood flow in human right coronary arteries: steady state simulations*, Journal of biomechanics, 37(5), 709-720, 2001

[4] M. Abbasian, M. Shams, Z. Valizadeh, A. Moshfegh, A. Javadzadegan, *Effect of non-newtonian blood flow on coronary artery hemodynamics in a cohort of patients with stenosed artery*, American society of mechanical engineers, 51555, V001T02A006, 2018.

[5] R. Torii, M. Oshima, T. Kobayashi, K. Takagi, T. E. Tezduyar, *Computer modeling of cardiovascular fluid–structure interactions with the deforming-spatial-domain/stabilized space–time formulation*, Computer methods in applied mechanics and engineering, 195, 13-16, 2006.

[6] T. J. Pedley, *The fluid mechanics of large blood vessels*, Cambridge university press, 1980.

[7] M. Girfoglio, F. Ballarin, G. Infantino, F. Nicol, A. Montalto, G. Rozza, R. Scrofani, M. Comisso, F. Musumeci, *Non-intrusive PODI-ROM for patient-specific aortic blood flow in presence of a LVAD device*, arXiv:2007.03527, 2020.

[8] F. Ballarin, E. Faggiano, A. Manzoni, A. Quarteroni, G. Rozza, S. Ippolito, C. Antona, R. Scrofani, *Numerical modeling of hemodynamics scenarios of patient-specific coronary artery bypass grafts*, Biomechanics and modeling in mechanobiology, 16(4), 1373-1399, 2017.

[9] F. Ballarin, E. Faggiano, S. Ippolito, A. Manzoni, A. Quarteroni, G. Rozza, R. Scrofani, *Fast simulations of patient-specific haemodynamics of coronary artery bypass grafts based on a POD–Galerkin method and a vascular shape parametrization*, Journal of computational physics, 315, 609-628, 2016.

[10] F. Ballarin, E. Faggiano, A. Manzoni, A. Quarteroni, G. Rozza, S. Ippolito, C. Antona, R. Scrofani, *Numerical modeling of hemodynamics scenarios of patient-specific coronary artery bypass grafts*, Biomechanics and modeling in mechanobiology, 16(4), 1373-1399, 2017.

[11] T. Lassila, A. Manzoni, A. Quarteroni, G. Rozza, *A reduced computational and geometrical framework for inverse problems in hemodynamics*, International journal for

numerical methods in biomedical engineering, 29(7), 741-776, 2013.

[12] A. Manzoni, A. Quarteroni, G. Rozza, *Model reduction techniques for fast blood flow simulation in parametrized geometries*, International journal for numerical methods in biomedical engineering, 28(6-7), 604-625, 2012.

[13] A. Manzoni, A. Quarteroni, G. Rozza, *Shape optimization for viscous flows by reduced basis methods and free-form deformation*, International journal for numerical methods in fluids, 70(5), 646-670, 2012.

[14] G. Pitton, A. Quaini, G. Rozza, *Computational reduction strategies for the detection of steady bifurcations in incompressible fluid-dynamics: applications to coanda effect in cardiology*, Journal of computational physics, 344, 534-557, 2017.

[15] F. Ballarin, A. Manzoni, A. Quarteroni, G. Rozza, *Supremizer stabilization of POD–Galerkin approximation of parametrized steady incompressible Navier–Stokes equations*, International journal for numerical methods in engineering, 102(5), 1136-1161, 2015.

[16] Z. Zainib, F. Ballarin, S. Fremes, P. Triverio, L. Jiménez-Juan, G. Rozza, *Reduced order methods for parametric optimal flow control in coronary bypass grafts, toward patient-specific data assimilation*, International journal for numerical methods in biomedical engineering, e3367, 2020.

[17] E. Fevola, F. Ballarin, L. Jiménez-Juan, S. Fremes, S. Grivet-Talocia, G. Rozza, P. Triverio, *An optimal control approach to determine resistance-type boundary conditions from in-vivo data for cardiovascular simulations*, arXiv:2104.13284, 2021.

[18] S. Schneiderbauer, M. Krieger, *What do the Navier-Stokes equations mean?*, European journal of physics, 35(1), 015020, 2014.

[19] S. Lanzoni, *Le equazioni della meccanica dei fluidi*, Dipartimento di ingegneria idraulica, marittima e geotecnica, Università di Padova.

[20] M. Gad-el-Hak, *Stokes' hypothesis for a newtonian, isotropic fluid*, Journal of fluids engineering, 117(3), 5, 1995.

[21] A. Quarteroni, *Le equazioni di Navier-Stokes*, Springer, 441-494, 2012.

[22] I. Ogobuiro, C. J. Wehrle, F. Tuma, *Anatomy, thorax, heart coronary arteries*, StatPearls, 2020.

[23] T. N. James,G. E. Burch, *Blood supply of the human interventricular septum*, Circulation, 17(3), 391-396, 1958.

[24] F. Revault d'Allonnes, H. Corbineau, H. Le Breton, C. Leclercq, A. Leguerrier, C. Daubert, *Isolated left main coronary artery stenosis: long term follow up in 106 patients after surgery*, Interventional cardiology and surgery, 87(6), 544-548, 2002.

[25] R. Scott, E. H. Blackstone, P. M. McCarthy, B. W. Lytle, F. D. Loop, J. A. White, D. M. Cosgrove, *Isolated bypass grafting of the left internal thoracic artery to the left anterior descending coronary artery: late consequences of incomplete revascularization*, American association for thoracic surgery, 120(1), 173-184, 2000.

[26] L. Harling, A. H. Sepehripour, H. Ashrafian, T. Lane, O. Jarral, J. Chikwe, R. A. E. Dion, T. Athanasiou, *Surgical patch angioplasty of the left main coronary artery*, European journal of cardio-thoracic surgery, 42(4), 719-727, 2012.

[27] M. Gaudino, M. Massetti, P. Farina, C. Hanet, P.Etienne, A. Mazza, D. Glineur, *Chronic competitive flow from a patent arterial or venous graft to the circumflex system does not impair the long-term patency of internal thoracic artery to left anterior*

descending grafts in patients with isolated predivisional left main disease: Long-term angiographic results of 2 different revascularization strategies, Journal of thoracic and cardiovascular surgery, 148(5), 1856-1859, 2014.

[28] J. M. Rosenblum, J. Binongo, J. Wei, Y. Liu, B. G. Leshnower, E. P. Chen, J. S. Miller, S. K. Macheers, O. M. Lattouf, R. A. Guyton, V. H. Thourani, M. E. Halkos, W. B. Keeling, *Priorities in coronary artery bypass grafting: is midterm survival more dependent on completeness of revascularization or multiple arterial grafts?*, Journal of thoracic and cardiovascular surgery, 2020.

[29] A. J. Rastan, *Treatment of coronary artery disease: randomized trials on myocardial revascularization and complete arterial bypass grafting*, Journal of thoracic and cardiovascular surgery, 65(S 03), S167-S173, 2017.

[30] F. Moukalled, L. Mangani, M. Darwish, *The finite volume method in computational fluid dynamics*, Springer, 113, 2015.

[31] H. Jasak, *Error analysis and estimation for the finite volume method with applications to fluid flows*, PhD thesis, Department of mechanical engineering, Imperial college of science, technology and medicine, 1996.

[32] R. Pandey, M. Kumar, V. K. Srivastav, *Numerical computation of blood hemodynamic through constricted human left coronary artery: pulsatile simulations*, Computer methods and programs in biomedicine, 197, 105661, 2020.

[33] A. Marsden, E. Kung, *Multiscale modeling of cardiovascular flows*, Computational bioengineering, 67(3), 2017.

[34] R. Pandey , M. Kumar , J. Majdoubi , M. Rahimi-Gorji , V. K. Srivastav, *A review study on blood in human coronary artery: numerical approach* , Computer methods and programs in biomedicine, 187, 105243, 2019.

[35] R. I. Issa, *Solution of the implicitly discretised fluid flow equations by operator-splitting* , Journal of computational physics, 62(1), 40-65, 1985.

[36] F. Ballarin, *Reduced-order model for patient-specific haemodynamic of coronary artery bypass grafts*, PhD thesis, Dipartimento di matematica, Politecnico di Milano, 2015.

[37] A. Mahalingam, U. U. Gawandalkar, G. Kini, A. Buradi, T. Araki, N. Ikeda, A. Nicolaides, J. R. Laird, L. Saba, J. S. Suri, *Numerical analysis of the effect of turbulence transition on the hemodynamic parameters in human coronary arteries*, Cardiovascular diagnosis and therapy, 6(3), 208, 2016.

[38] M. D. Deshpande, *Steady laminar and turbulent flow through vascular stenosis models*, PhD thesis, Georgia Institute of Technology, 1977.

[39] M. Bathe, R. D. Kamm, *A fluid-structure interaction finite element analysis of pulsatile blood flow through a compliant stenotic artery*, Journal of biomechanical engineering, 121(4), 361-369, 1999.

[40] W. Chen, Q. Wang, J. S. Hesthaven, C. Zhang, *Physics-informed machine learning for reduced-order modeling of non linear problems* , Preprint, 2020.

[41] P. Benner, S. Gugercin, K. Willcox, *A survey of projection-based model reduction methods for parametric dynamical systems*, Society for industrial and applied mathematics, 57(4), 483-531, 2015.

[42] J. S. Hesthaven, S. Ubbiali, *Non-intrusive reduced order modeling of nonlinear problems using neural networks*, Journal of computational physics, 363, 55-78, 2018.

[43] J. S. Hesthaven, G. Rozza, B. Stamm, *Certified reduced basis methods for parametrized equations*, Springer, 590, 2016.

[44] R. Falcone, O. Capirci, F. Lucidi, P. Zoccolotti, *Prospettive di intelligenza artificiale: mente, lavoro società nel mondo del machine learning*, Giornale italiano di psicologia, 45(1), 43-68, 2018.

[45] J. Bang-Jensen, G. Gutin, A. Yeo, *When the greedy algorithm fails*, Discrete optimization, 1(2), 121-127, 2004.

[46] C. Eckart, G. Young, *The approximation of one matrix by another of lower rank*, Psychometrika, 1(3), 211-218, 1936.

[47] D. P. Berrar, W. Dubitzky, M. Granzow, *A practical approach to microarray data analysis*, Springer, 2003.

[48] S. Sharma, S. Sharma, A. Athaiya, *Activation functions in neural networks*, Towards data science, 6(12), 310-316, 2020.

[49] D. J. Montana, L. Davis, *Training feedforward neural networks using genetic algorithms* , International joint conferences on artificial intelligence organization, 89, 762-767, 1989.

[50] D. E. Rumelhart, G. E. Hinton, R. J. Williams, *Learning representations by back-propagating errors*, Nature, 323(6088), 533-536, 1986.

[51] S. Ioffe, C. Szegedy, *Batch normalization: Accelerating deep network training by reducing internal covariate shift*, International conference on machine learning, 448-456, PMLR, 2015.

[52] J. Keegan, P. D. Gatehouse, G. Z. Yang, D. N. Firmin, *Spiral phase velocity mapping of left and right coronary artery blood flow: correction for through-plane motion using selective fat-only excitation*, Journal of magnetic resonance imaging, 20(6), 953-960, 2004.

[53] N. Ishida, H. Sakuma, B. P. Cruz, T. Shimono, T. Tokui, I. Yada, K. Takeda, C. B. Higgins, *MR flow measurement in the internal mammary artery– to–coronary artery bypass graft: comparison with graft stenosis at radiographic angiography*, Radiology, 220(2), 441-447, 2001.

[54] S. Verim, E. Öztürk, U. Küçük, K. Kara, M. Sağlam, E. Kardeşoğlu, *Cross-sectional area measurement of the coronary arteries using CT angiography at the level of the bifurcation: is there a relationship?*, Diagnostic interventional radiology journal, 21(6), 454, 2015.

[55] L. Liang, W. Mao, W. Sun, *A feasibility study of deep learning for predicting hemodynamics of human thoracic aorta*, Journal of biomechanics, 99, 109544, 2020.

[56] R. Gharleghi, G. Samarasinghe, A. Sowmya, S. Beier, *Deep learning for time averaged wall shear stress prediction in left main coronary bifurcations*, International symposium on biomedical imaging, 1-4, 2020.

[57] Z. Mao, A.D. Jagtap and G.E. Karniadakis, *Physics-informed neural networks for high-speed flows*, Computer methods in applied mechanics and engineering, 360, 112789, 2020.

[58] B. Su, J. Zhang, H. Zou, D. Ghista, T. Thao Le, C. Chin, *Generating wall shear stress for coronary artery in real-time using neural networks: feasibility and initial results based on idealized models*, Computers in biology and medicine, 126, 104038, 2020

[59] G. Kissas, Y. Yang, E. Hwuang, W. R. Witschey, J. A. Detre, P. Perdikaris, *Machine learning in cardiovascular flows modeling: predicting arterial blood pressure from non-invasive 4D flow MRI data using physics-informed neural networks*, Computer methods in applied mechanics and engineering, 358, 112623, 2019.

[60] T. M. Razakh, B. Wang, S. Jackson, R. K. Kaila, A. Nakano, K. Nomura, P. Vashishta, *Physics-informed neural-network software for molecular dynamics applications*, arXiv:2011.03490, 2020.